

RESEARCH ARTICLE

Actin network disassembly powers dissemination of *Listeria monocytogenes*

 Arthur M. Talman¹, Ryan Chong¹, Jonathan Chia², Tatyana Svitkina² and Hervé Agaisse^{1,*}
ABSTRACT

Several bacterial pathogens hijack the actin assembly machinery and display intracellular motility in the cytosol of infected cells. At the cell cortex, intracellular motility leads to bacterial dissemination through formation of plasma membrane protrusions that resolve into vacuoles in adjacent cells. Here, we uncover a crucial role for actin network disassembly in dissemination of *Listeria monocytogenes*. We found that defects in the disassembly machinery decreased the rate of actin tail turnover but did not affect the velocity of the bacteria in the cytosol. By contrast, defects in the disassembly machinery had a dramatic impact on bacterial dissemination. Our results suggest a model of *L. monocytogenes* dissemination in which the disassembly machinery, through local recycling of the actin network in protrusions, fuels continuous actin assembly at the bacterial pole and concurrently exhausts cytoskeleton components from the network distal to the bacterium, which enables membrane apposition and resolution of protrusions into vacuoles.

KEY WORDS: *Listeria*, ARP2/3, Actin assembly, Actin network disassembly, AIP1, WDR1, CFL1, GMFB

INTRODUCTION

Several intracellular pathogens, including *Listeria monocytogenes*, *Shigella flexneri*, *Rickettsia* spp. and *Burkholderia* spp. exploit the host cell actin cytoskeleton to spread from cell to cell through the formation of membrane protrusions that resolve into double membrane vacuoles in neighboring cells (Haglund and Welch, 2011; Lambrechts et al., 2008; Stevens et al., 2006). The molecular mechanisms supporting actin-based motility have been deciphered using *L. monocytogenes* as a model system. Genetic investigations have led to the identification of ActA as a bacterial factor required for the polymerization of actin on the surface of cytosolic bacteria (Domann et al., 1992; Kocks et al., 1992). Biochemical studies have uncovered the central role of the ARP2/3 complex as a host cell actin nucleator in *L. monocytogenes* actin tail assembly (Welch et al., 1997). Combined genetic and biochemical approaches have established that ActA mimics the activity of WASP and WAVE family members, which bind the ARP2/3 complex and promote its nucleation activity (Lasa et al., 1997; Skoble et al., 2000; Welch et al., 1997; Welch et al., 1998). The actin network formed by the ARP2/3 complex is composed of short and branched filaments resulting from

the binding of the complex to existing mother filaments and the nucleation of daughter filaments whose brief elongation is terminated by capping proteins (Pollard and Borisy, 2003). The expansion of the actin network formed on the surface of intracellular pathogens generates forces that propel the bacteria through the cytosol. *In vitro* reconstitution experiments have revealed that, in addition to the ARP2/3 complex, actin-based motility requires the presence of capping proteins and the actin-filament-severing protein cofilin, which are thought to be necessary to maintain a high-steady state level of G-actin (Loisel et al., 1999). In addition, motility is more effective in presence of profilin, α -actinin and VASP (Loisel et al., 1999). Experiments using thymus extracts have also revealed the cooperative role of cofilin, AIP1 and coronin in the disassembly of *L. monocytogenes* actin tails *in vitro* (Briehier et al., 2006).

In contrast to the mechanisms supporting cytosolic motility, the mechanisms supporting formation of membrane protrusions are poorly understood. The sequence and timing of the cellular events supporting *L. monocytogenes* spread from cell to cell, including the formation of membrane protrusions and their resolution into double membrane vacuoles, have been established by time-lapse microscopy (Robbins et al., 1999). After a short elongation phase, protrusions display little or no movement for variable periods of time, before they are resolved into vacuoles. The exact mechanisms supporting the elongation of the formed protrusions and their resolution into vacuoles in the neighboring cells are unknown. Structural analyses of the actin network formed in *L. monocytogenes* protrusions have revealed that, as opposed to the short and branched filaments observed in cytosolic tails, membrane protrusions harbor long and bundled filaments (Sechi et al., 1997). Moreover, the actin cytoskeleton factors present, such as α -actinin and ezrin, are different in cytosolic tails and in protrusions (Sechi et al., 1997). Furthermore, functional studies have revealed that there are host factors, such as the serine/threonine kinase CSNK1, that are dispensable for *L. monocytogenes* cytosolic motility, but required for protrusion resolution into vacuoles (Chong et al., 2011). Taken together, these observations indicate that, in spite of the fact that the minimal set of cellular factors required for reconstituting actin-based motility *in vitro* has been clearly defined (Loisel et al., 1999), the cellular processes supporting cell-to-cell spread through protrusion formation remain to be determined.

Here, we investigate the cytoskeleton factors required for *L. monocytogenes* spread from cell to cell. We uncover a crucial role for the actin network disassembly machinery in the formation and resolution of membrane protrusions.

RESULTS
Identification of host factors required for *L. monocytogenes* dissemination

To uncover cellular factors supporting *L. monocytogenes* dissemination, we developed a microscopy-based assay for

¹Department of Microbial Pathogenesis, Boyer Center for Molecular Medicine, Yale School of Medicine, New Haven, CT 06536, USA. ²Department of Biology, University of Pennsylvania, Philadelphia, PA 19104, USA.

*Author for correspondence (herve.agaisse@yale.edu)

quantifying the spread of GFP-expressing bacteria in a given infection focus (Fig. 1). The assay relied on the identification of spreading bacteria that tend to be scattered (Fig. 1A, Individual), as opposed to non-spreading bacteria that tend to be clustered (Fig. 1A, Clustered bacteria). We defined the spreading index as the proportion of the GFP signal corresponding to spreading bacteria in a given infection foci. We used inhibitors of the actin cytoskeleton to demonstrate that this approach allowed for the quantification of a large range of spreading defects (Fig. 1B). We next used the spreading assay to screen a siRNA library targeting genes encoding regulators of the actin cytoskeleton (Siripala and Welch, 2007) (supplementary material Table S1). The library harbored four independent siRNA duplexes targeting a given gene. We defined hits as genes for which at least two siRNA duplexes conferred spreading index values that deviated by at least 2 standard deviation units from the mean spreading index value observed in mock-treated cells. According to these selection criteria, we identified eight cytoskeleton factors required for *L. monocytogenes* dissemination, including components of the ARP2/3 complex, such as ARPC4, the capping protein CAPZB and the actin interacting protein 1 (AIP1, also known as WD repeat-containing protein 1, WDR1) (supplementary material Table S1, 25 nM). The specificity of the observed spreading defects was confirmed by using four independent silencing duplexes (supplementary material Table S1) and their silencing efficiency was determined at the mRNA and protein levels (supplementary material Fig. S1).

Host factors required for cytosolic motility

In vitro reconstitution experiments have previously established that *L. monocytogenes* motility relies on the ARP2/3 complex, capping proteins and the actin-depolymerizing factor (ADF) family member cofilin-1 (CFL1) (Loisel et al., 1999). Validating our *in vivo* genetic screen, we identified components of the ARP2/3 complex, such as ARPC4 and the capping protein CAPZB (Fig. 2A,B). We failed to identify CFL1; however, we identified AIP1 (Fig. 2A,B, AIP1), a component of the actin

network disassembly machinery that acts as a co-factor of CFL1 (Poukkula et al., 2011). To clarify the role of CFL1 and AIP1 in cytosolic motility, we determined the length of the actin tails formed in the cytosol of infected cells (supplementary material Fig. S2A). As expected for components of the disassembly machinery, we found that CFL1 or AIP1 depletion resulted in a significant increase in the length of the formed actin tails (Fig. 2C). However, the proportion of bacteria associated with F-actin (Fig. 2D) and the velocity of motile bacteria (Fig. 2E), were not affected in the cytosol of mock-treated, CFL1- or AIP1-depleted cells. We also found that co-depleting CFL1 and AIP1 resulted in a significant increase in the length of the formed actin tails (Fig. 2C), but marginally affected bacterial velocity (Fig. 2E). Finally, we localized GFP–AIP1 and CFL1–GFP to cytosolic actin comet tails (Fig. 2F). These results indicate that the CFL1 and AIP1 machinery mediates the disassembly of *L. monocytogenes* cytosolic tails *in vivo*, as suggested previously in *in vitro* studies (Brieher et al., 2006). However, the depletion of the components of the disassembly machinery had little impact on the bacterial velocity, probably because the actin supply in the cytosol of cells impaired for actin network disassembly was sufficient to support wild-type actin assembly at the bacterial pole.

A role for the AIP1 and CFL1 disassembly machinery in protrusion and vacuole formation

Because the cytosolic velocity of motile bacteria was not affected in AIP1-depleted cells (Fig. 2E) and yet the bacteria failed to spread from cell to cell (Fig. 2A,B), we hypothesized that defects in the AIP1-dependent disassembly machinery might lead to defects in protrusion and/or vacuole formation. As shown in supplementary material Movie 1, *L. monocytogenes* forms membrane protrusions that initially elongate for a short period of time (5–10 minutes) and then display slow or no motion for variable periods of time (30–60 minutes), followed by sudden resolution into vacuoles, as previously reported (Robbins et al., 1999). We determined that AIP1 depletion led to a significant

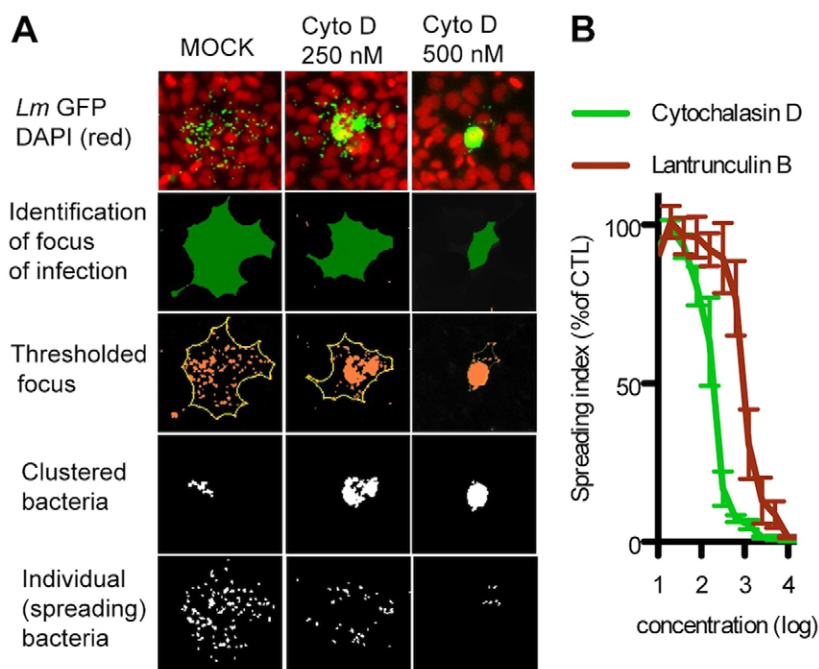


Fig. 1. Computer-assisted image analysis of *L. monocytogenes* spread from cell to cell.

(A) Representative examples of infection foci for mock-treated and Cytochalasin D (Cyto D) treatments (250 and 500 nM) 8 hours after infection, inhibitors were added 1 hour post-infection. (B) Titration experiments with two inhibitors of actin assembly (cytochalasin D or Lantrunculin B) showing the effect of inhibitor concentration and spreading index.

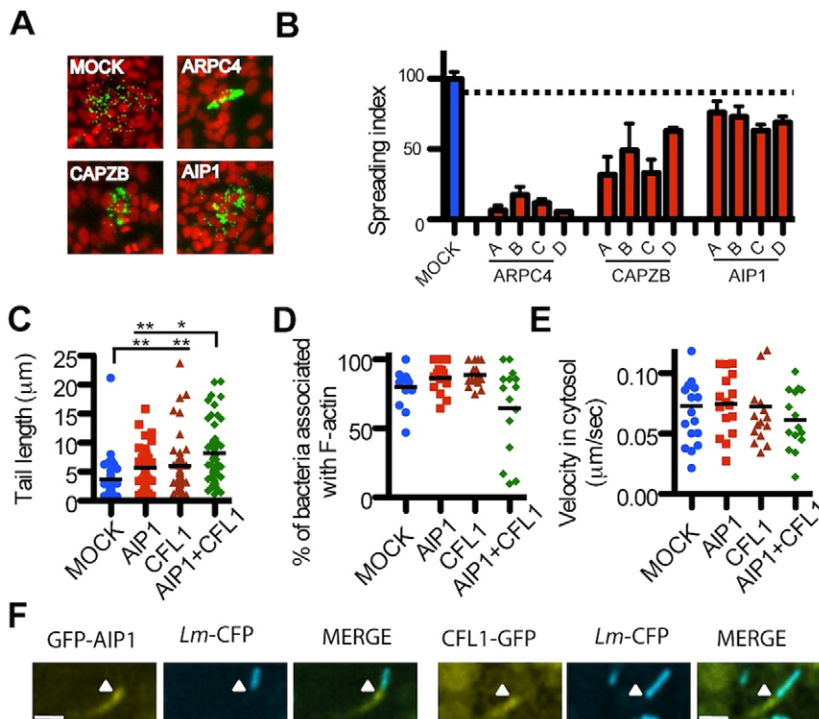


Fig. 2. RNAi screen for host factors involved in *L. monocytogenes* dissemination. (A) Images of infection foci in mock-treated (MOCK), and ARPC4-, CAPZB- and AIP1-depleted cells, after 8 hours of infection with GFP-expressing *L. monocytogenes* (green) and stained with DAPI (red). (B) Quantification of spreading index in cells transfected with four independent siRNA duplexes (labeled A, B, C and D) targeting ARPC4, CAPZB or AIP1. Data are presented as mean \pm s.e.m. of three independent experiments. The dashed line indicates the threshold corresponding to 2 s.d. units. (C,D) Length of actin tails (C), and proportion of actin-associated bacteria (D) (supplementary material Fig. S2) in the cytosol of cells in which the disassembly components, cofilin-1 (CFL1) and AIP1 have been depleted alone or in combination (Tail length: MOCK vs AIP1, $P=0.0043$; MOCK vs CFL1, $P=0.0033$; AIP1 versus AIP1 + CFL1, $P=0.00298$; CFL1 versus AIP1+CFL1, $P=0.0356$; Mann-Whitney U test). (E) Cytosolic velocity of bacteria (MOCK versus AIP1, $P=0.7431$; MOCK versus CFL1, $P=0.7791$; AIP1 versus AIP1+CFL1, $P=0.2131$; CFL1 versus AIP1+CFL1, $P=0.4731$; Mann-Whitney U test) (F) Cells were co-transfected with constructs expressing GFP-AIP1 or CFL1-GFP, and infected with CFP-expressing *L. monocytogenes*. AIP1 and CFL1 are enriched in the cytosolic tail. * $P\leq 0.05$; ** $P\leq 0.01$; *** $P\leq 0.001$.

decrease in the velocity of bacteria in protrusions (Fig. 3A, AIP1). We then quantified protrusion and vacuole formation (supplementary material Fig. S2B), as previously described (Chong et al., 2011). We determined that AIP1 depletion led to an increase in the number of protrusions (Fig. 3B, AIP1 versus

Mock, protrusions) that correlated with a decrease in the number of bacteria gaining access to the cytosol of adjacent cells (Fig. 3B, AIP1 versus Mock, free). To confirm the specificity of the observed phenotype, we rescued AIP1 silencing by using RNAi-resistant constructs expressing wild-type or mutant

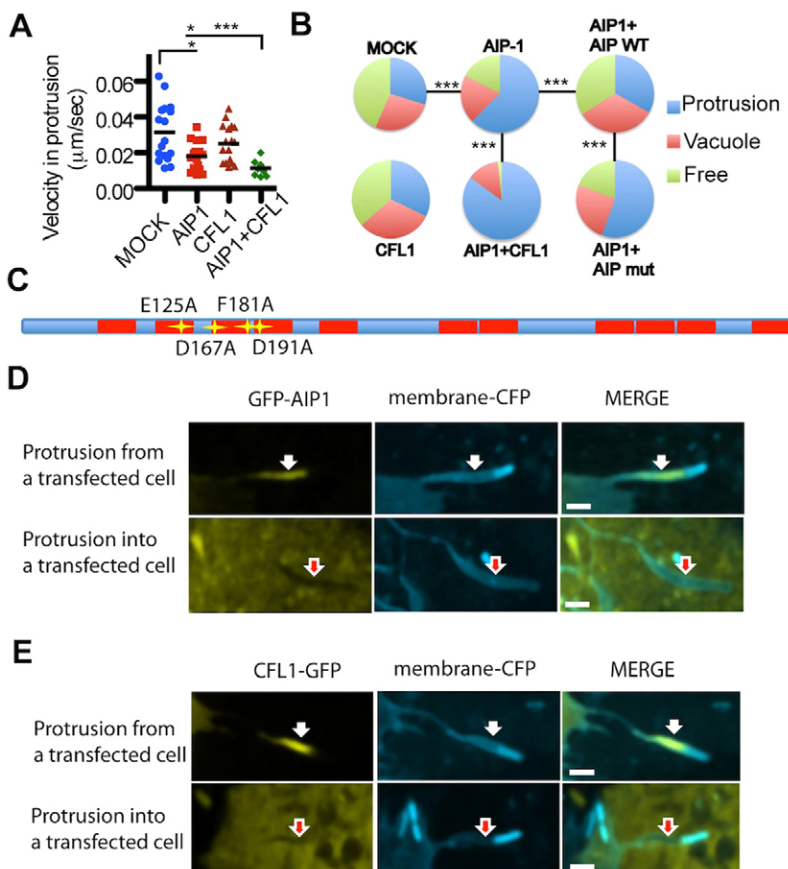


Fig. 3. Function and localization of AIP1 and CFL1 in protrusions. (A) Velocity of elongating protrusions in mock-treated (MOCK), and ARPC4-, CAPZB- and AIP1-depleted cells (MOCK versus AIP1, $P=0.0202$; MOCK versus CFL1, $P=0.2985$; AIP1 versus AIP1+CFL1, $P=0.0309$; CFL1 versus AIP1+CFL1, $P<0.0001$; Mann-Whitney U test). (B) Proportion of bacteria found in protrusions, vacuoles or free in the cytosol of neighboring cells as shown in supplementary material Fig. S3B. Cells were either mock-treated or AIP1+CFL1-depleted, in addition AIP1-depleted cells were transfected with siRNA-resistant rescue constructs expressing wild type (AIP1 +AIPWT) or depolymerization-deficient AIP1 (AIP1+AIPmut). Data are representative of three independent experiments. Proportion of protrusions: MOCK versus AIP1, $P=0.0001$; MOCK versus CFL1, $P=0.2380$; AIP1 versus AIP1+CFL1, $P=0.0001$; AIP1 versus AIP1+AIPWT, $P=0.0001$; AIP1+AIPWT versus AIP1+AIPmut, $P=0.0004$. Proportion of free bacteria in secondary cell: MOCK versus AIP1, $P<0.0001$; MOCK versus CFL1, $P=0.2270$; AIP1 versus AIP1+CFL1, $P<0.0001$; AIP1 versus AIP1+AIPWT, $P=0.0032$; AIP1+AIPWT versus AIP1+AIPmut, $P=0.0064$. All P -values are calculated using the Mann-Whitney U test. (C) Schematic representation of the AIP-1 protein. Red boxes represent WD40 domains. The position of amino acids that were mutagenized in the depolymerization-deficient mutant form of AIP1 are marked by a yellow star. (D,E) Cells were co-transfected with constructs expressing (D) membrane-targeted CFP and GFP-AIP1 or (E) membrane-targeted CFP and CFL1-GFP, and infected with CFP-expressing *L. monocytogenes*. AIP1 and CFL1 are enriched in the protrusion when the sending cells is transfected (white arrows). AIP1 and CFL1 are not enriched on the protrusion when the receiving cell is transfected (red arrows). Scale bars: 2 μ m. * $P\leq 0.05$; ** $P\leq 0.01$; *** $P\leq 0.001$.

versions of AIP1 (Fig. 3C) (Mohri et al., 2006). These results showed that the rescue of the observed defects required the activity of AIP1 in the cell that formed the protrusions (Fig. 3B, AIP1 + AIP1 WT, and AIP1 + AIP1 mut). Accordingly, we found that GFP–AIP1 was enriched in protrusions when expressed in the sending cell, but was not recruited to protrusions when expressed in the receiving cell (Fig. 3D). We also established that co-depletion of AIP1 and CFL1 dramatically affected the velocity of bacteria in protrusions (Fig. 3A, AIP1 + CFL1) and the resolution of protrusion into vacuoles (Fig. 3B, AIP1 + CFL1). Similar to GFP–AIP1, CFL1–GFP was also enriched in protrusions (Fig. 3E). Taken together, these experiments uncover a crucial role for the AIP1 and CFL1 actin network disassembly machinery in protrusion and vacuole formation.

The ARP2/3 complex is recycled in protrusions

To further understand the role of actin network disassembly in *L. monocytogenes* protrusions, we compared the structural and dynamic organization of the actin network in cytosolic tails and in membrane protrusions. *L. monocytogenes* forms a branched network relying on the incorporation of the ARP2/3 complex, resulting in a distribution of actin and ARP2/3 more intense proximal to the bacterium and slowly decreasing along cytosolic tails (Fig. 4A, Cytoplasm, and Fig. 4B).

The distribution of actin and ARP2/3 in elongating protrusions was similar in the network proximal to the bacterial pole (Fig. 4A, Protrusion, and Fig. 4C). However, analyses of the network distal to the bacterial pole revealed a dramatic depletion of ARP2/3 with respect to actin (Fig. 4A, Protrusion, and Fig. 4C). Time-lapse microscopy revealed that the ARP2/3-containing network formed at the bacterial pole was subsequently remodeled into an ARP2/3-devoid distal network during protrusion elongation (Fig. 4D, and supplementary material Movie 2). In agreement with this notion, electron microscopy images of protrusions demonstrated the presence of a branched network at the bacterial pole along with variable amounts of long and bundled filaments (Fig. 4E, proximal). This was in contrast with the distal network, which was essentially composed of long and bundled filaments (Fig. 4E, distal), as previously reported (Sechi et al., 1997). Fluorescence recovery after photo bleaching experiments (FRAP) revealed a minimal recovery of the pool of ARP2/3 located at the bacterial pole in protrusions, demonstrating very little contribution from the cytosol (supplementary material Fig. S3A). Collectively, these results demonstrate that protrusion elongation relies on a pool of ARP2/3 that is constantly recycled from the distal network and incorporated into the newly formed network at the bacterial pole.

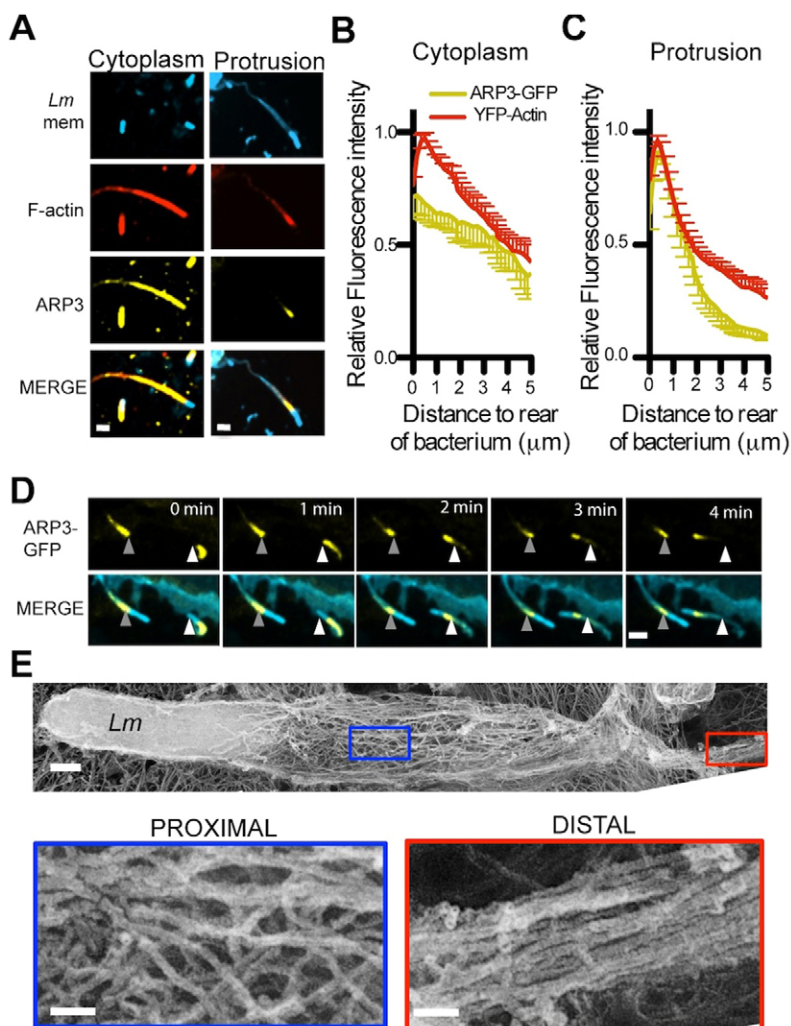


Fig. 4. Structural and dynamic organization of the actin network in cytosolic tails and protrusions.

(A) Representative images of the actin tail and protrusion formed in cells transfected with a membrane-targeted CFP-expressing construct and infected for 4 hours with CFP-expressing *L. monocytogenes*. Cells were stained for F-actin (red) and ARP3 (yellow). Scale bars: 2 μm . (B,C) Distribution of ARP3–GFP or YFP–actin independently assessed in cytosolic tails (B) or in elongating protrusions (>0.01 $\mu\text{m}/\text{second}$) (C), as determined by time-lapse microscopy. Data are mean \pm s.e.m. (D) Dynamics of ARP3–GFP in cells transfected with membrane-targeted CFP constructs and infected for 4 hours with CFP-expressing *L. monocytogenes*. Gray and white arrowheads mark a reference point on the stationary (left) and elongating (right) protrusions, respectively. Scale bar: 2 μm . (E) Replica electron micrograph of a *L. monocytogenes* (*Lm*)-induced protrusion; insets display the filament organization in the proximal (blue) and distal (red) networks. Scale bars: 200 nm (main), 50 nm (insets).

Actin network recycling in elongating protrusions

We further examined the dynamics of the actin network by using a photo-activatable version of GFP fused to mCherry-actin (Welman et al., 2010). In the cytosol, photo-activation of the distal region of an elongating actin tails produced a GFP signal that slowly decreased in intensity as the tail disassembled (Fig. 5A, white arrowhead in tiled images, red dashed line in kymograph; supplementary material Movie 3) (Theriot et al., 1992). In elongating protrusions, and similar to the situation observed in the cytosol, photo-activation of the distal network produced a GFP signal that slowly decreased in intensity at the site of photo-activation (Fig. 5B, white arrowhead in tiled images, red dashed line in kymograph; supplementary material

Movie 4). In contrast with the situation observed in the cytosol (Fig. 5A), we observed the appearance of a signal at the bacterial pole that increased in intensity as protrusions elongated (Fig. 5B, blue arrowhead in tiled images, black dashed line in kymograph; supplementary material Movie 4). Measurement of the diffusion rate of photo-activatable free GFP and GFP-actin in protrusions (supplementary material Fig. S3B–D) and treatment with actin polymerization inhibitors (supplementary material Fig. S3E) revealed that (1) the disappearance of photo-activated molecules at the site of photo-activation reflects actin network disassembly, and (2) the accumulation of photo-activated molecules at the bacterial pole, reflects actin assembly. In addition, FRAP experiments with GFP and GFP-actin indicated

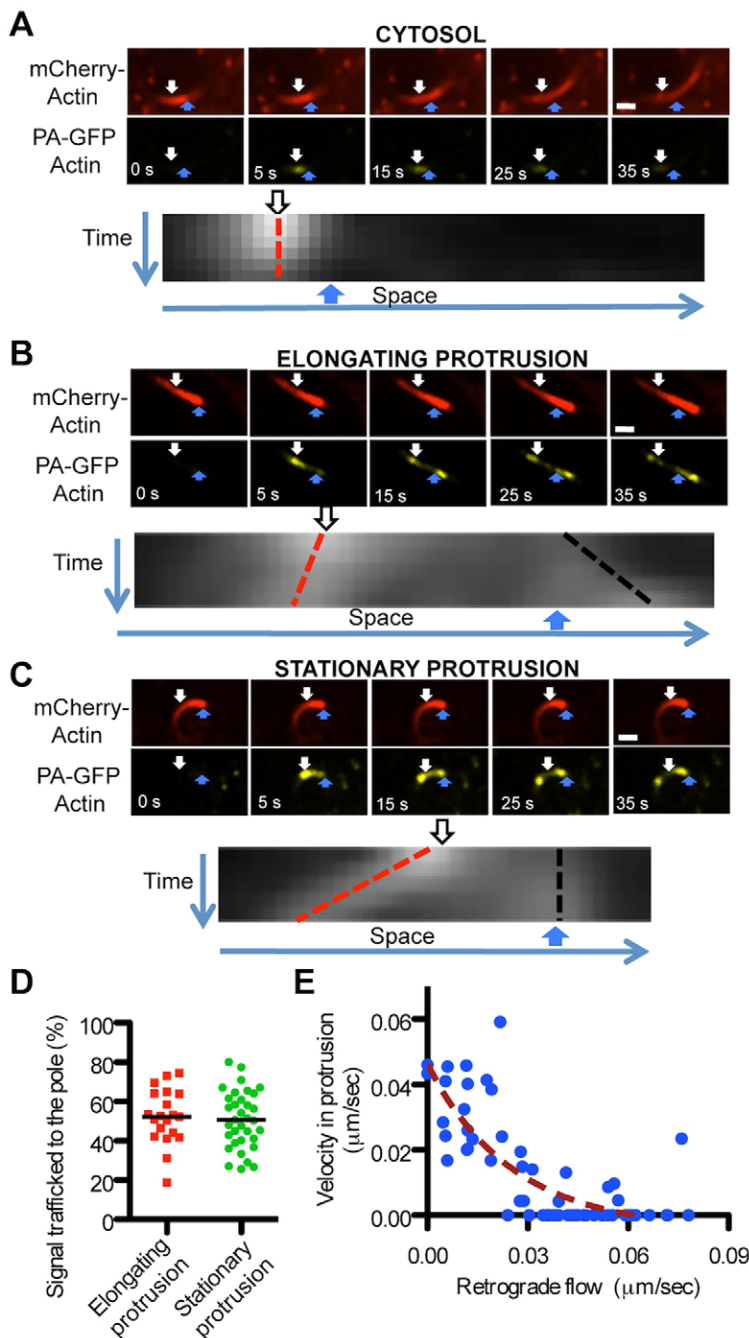


Fig. 5. Disassembly of the distal network in *L. monocytogenes* protrusions fuels actin assembly at the bacterial pole.

(A–C) Time-lapse imaging of photo-activation of β -actin fused to mCherry and photo-activatable GFP in a cytosolic tail (A), an elongating protrusion (B) and a stationary protrusion (C). White arrows indicate the site of photo-activation and blue arrows indicate the initial position of the bacterial pole. Scale bar: 2 μm . Kymographs represent the evolution of the photo-activated signal over space (x-axis) and time (y-axis). Red dashed lines indicate the progression of the signal from the initial site of photo-activation and black dashed lines indicate the signal evolution at the bacterial pole. (D) Percentage of the initial photo-activated signal trafficked to the bacterial pole after 35 seconds in elongating and stationary protrusions ($<0.01 \mu\text{m}/\text{s}$) (stationary versus elongating, $P=0.6097$, Mann–Whitney U test). (E) Negative correlation of elongation rate and retrograde flow in protrusions ($R=-0.7375$, $P<0.0001$, Spearman's rank correlation).

very slow recovery of the pool of actin in protrusions, confirming the notion that protrusions constitute a confined environment (supplementary material Fig. S3A). Thus, similar to the situation observed with ARP2/3, these experiments indicate that actin molecules are recycled from the distal network in the confined environment of protrusions and fuel assembly of the network proximal to the bacterial pole in elongating protrusions.

Actin network recycling in stationary protrusions

In addition to elongating protrusions, we also examined the dynamics of the actin network in protrusions that became stationary after their elongating phase and before their resolution into vacuoles. Unexpectedly, we found that, in those protrusions that displayed little or no movement (Fig. 5C, blue arrowhead in tiled images, black dashed line in kymograph; supplementary material Movie 5), the rate of actin assembly was similar to the rate observed in elongating protrusions (Fig. 5D). In addition, as the corresponding signal decreased in intensity, photo-activated molecules drifted away, as a whole, from the site of photo-activation (Fig. 5C, white arrow in tiled images, red dashed line in kymograph; supplementary material Movie 5). These experiments revealed that, as a result of network assembly at the bacterial pole, the whole network was displaced backwards in stationary protrusions. In agreement with this notion, treatment with actin polymerization inhibitors dramatically affected actin assembly at the bacterial pole (supplementary material Fig. S3E) and the observed backward drift of the actin network (supplementary material Fig. S3F). We refer to this phenomenon as ‘retrograde flow in protrusions’, based on analogy to the actin retrograde flow observed in lamellipodia (Forscher and Smith, 1988; Pollard and Borisy, 2003; Wang, 1985). We further demonstrated an inverse correlation between elongation and retrograde flow in protrusions (Fig. 5E). Thus, actin assembly at the bacterial pole mediates (1) protrusion elongation with minimal retrograde flow during the initial period of protrusion formation, and (2) maximal retrograde flow in protrusions that no longer elongate.

AIP1- and CFL1-dependent recycling of the actin network in protrusions

We next investigated the role of the AIP1- and CFL1-dependent disassembly machinery in the dynamics of the actin network in protrusions. We determined that the distal region of the protrusions formed in AIP1- and AIP1- plus CFL1-depleted cells was wider (Fig. 6A,B), and displayed altered distribution of F-actin (Fig. 6A,C) and ARP2/3 (Fig. 6A,D), suggesting a role for the AIP1 and CFL1 disassembly machinery in the recycling of the distal network. We used the photo-activation assay to quantify the disappearance of photo-activated molecules at the site of photo-activation, as a measure of actin network disassembly, and accumulation of photo-activated molecules at the bacterial pole, as a measure of actin assembly. We found that the protrusions formed in AIP1- and AIP1- plus CFL1-depleted cells displayed slow actin network disassembly (Fig. 6E), which correlated with slow actin assembly at the bacterial pole (Fig. 6F). Thus, defects in the AIP1- and CFL1-dependent-machinery led to severe defects in the recycling of the actin network formed by the bacteria in protrusions, which dramatically affected actin assembly at the bacterial pole.

Identification of GMFB as a component of the AIP1-dependent disassembly machinery

To define additional components of the AIP1-dependent disassembly machinery, we screened the cytoskeleton library

for factors whose depletion would enhance the spreading defect phenotype displayed by AIP1-depleted cells. This approach confirmed the involvement of CFL1 and led to the identification of glial maturation factor β (GMFB), twinfilin 2 (TWF2) and adenylate cyclase-associated protein 1 (CAP1) (supplementary material Fig. S4 and Table S1, 25 nM+25 nM AIP1). The specificity of these genetic interactions (supplementary material Table S1) was confirmed by using various combinations of independent and validated silencing reagents (supplementary material Figs S1, S4). We further investigated the role of GMFB, which together with CFL1 and TWF2, is a member of the ADF family (Nakano et al., 2010). We found that, reminiscent of the situation observed in AIP1- plus CFL1-depleted cells, the distal region of the protrusions formed in AIP1- plus GMFB-depleted cells was wider (Fig. 6B) and displayed altered distribution of F-actin (Fig. 6A,C) and ARP2/3 (Fig. 6A,D). We also established that the protrusions formed in AIP1- plus GMFB-depleted cells displayed slow actin network disassembly (Fig. 6E), which correlated with slow actin assembly at the bacterial pole (Fig. 6F). We finally counted the membrane protrusions and double-membrane vacuoles in neighboring cells and determined that AIP1 plus GMFB depletion led to a dramatic accumulation of protrusions that correlated with a decrease in the number of bacteria gaining access to the cytosol of adjacent cells (Fig. 6G, free). Collectively, these results define GMFB as a component of the AIP1-dependent disassembly machinery required for local recycling of the actin network in protrusions, which is crucial for bacterial dissemination.

DISCUSSION

Seminal studies on *L. monocytogenes* have uncovered an essential role for the actin assembly machinery in actin-based motility. However, the cellular processes supporting bacterial spread from cell to cell have remained elusive. Here, we have uncovered an essential role for the disassembly machinery in the formation and resolution of membrane protrusions *in vivo*. On the basis of our findings, we propose the following model for how *L. monocytogenes* spreads from cell to cell. The bacterium first develops actin-based motility in the cytosol of infected cells and initiates protrusion formation as it encounters the plasma membrane. The AIP1-dependent disassembly machinery (Fig. 7A) then powers the elongation process by recycling the network formed by the bacterium, thereby fueling ARP2/3-dependent actin assembly at the bacterial pole (Fig. 7B). As the recycling process exhausts the cytoskeleton components from the distal network, protrusions become stationary, and actin assembly results in retrograde flow. Exhaustion of the cytoskeleton from the distal network together with the simultaneous generation of forces by actin assembly at the bacterial pole, and the resulting retrograde flow, allow for concerted membrane apposition and membrane tensions, that lead to membrane disruption and vacuole formation (Fig. 7C).

In addition to the mechanisms supporting bacterial dissemination, our work further establishes striking parallels between the cellular processes supporting the formation of *L. monocytogenes* protrusions and cellular structures, such as lamellipodia (Haglund and Welch, 2011; Lambrechts et al., 2008; Stevens et al., 2006). This includes the conserved role of essential components, such as AIP1 and CFL1 (Poukkula et al., 2011; Siripala and Welch, 2007), and the potent actin network retrograde flow resulting from actin assembly (Forscher and Smith, 1988). Importantly, our genetic investigations led to the

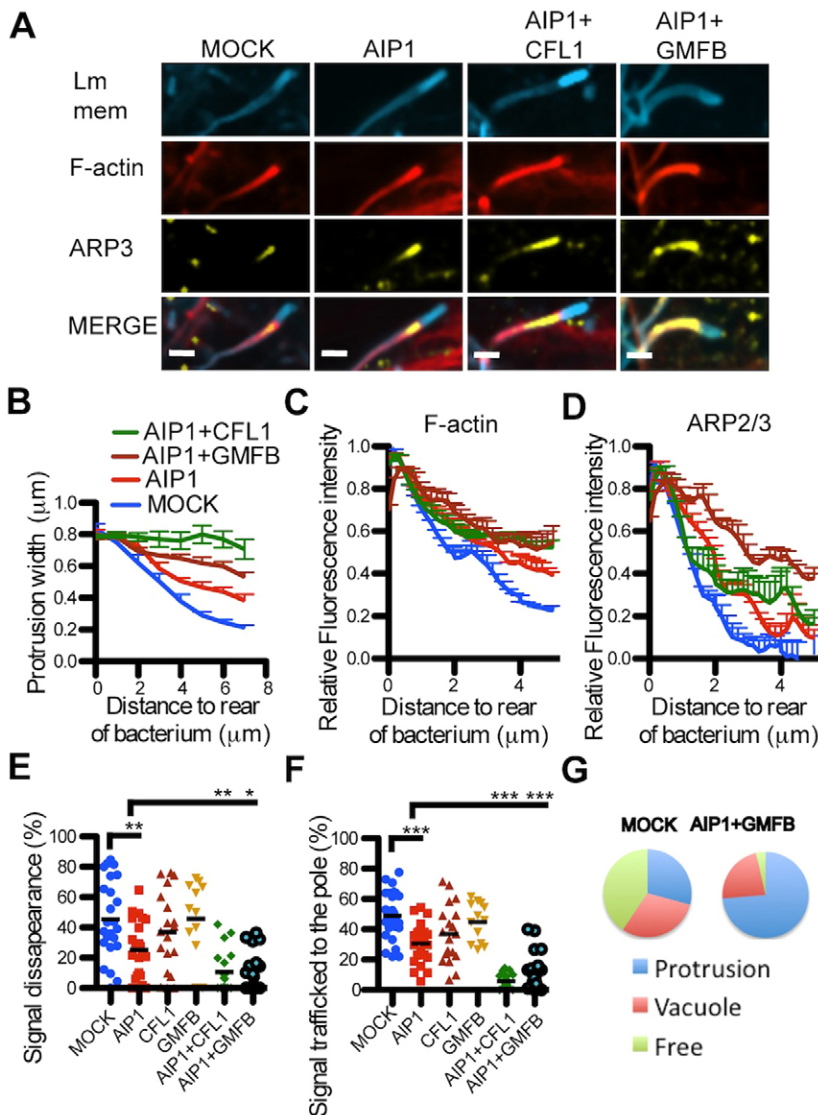


Fig. 6. Role of AIP1, CFL1 and GMFB in *L. monocytogenes* protrusions.

(A) Representative images of protrusions formed in mock-treated (MOCK), and AIP1-, AIP1+CFL1- or AIP1+GMFB-depleted cells transfected with a membrane-targeted CFP-expressing construct and infected for 4 hours with CFP-expressing *L. monocytogenes*. Scale bars: 2 μ m. (B–D) Width of protrusions (B), distribution of F-actin (C) and ARP2/3 (D) in protrusions as shown in A. Data are mean \pm s.e.m. (E) Percentage of signal disappearance of initial photo-activated signal after 35 seconds in mock-treated, AIP1-, AIP1+CFL1- or AIP1+GMFB-depleted cells (MOCK versus AIP1, $P=0.0016$; AIP1 versus AIP1+CFL1, $P=0.0077$; AIP1 versus AIP1+GMFB, $P=0.0365$; Mann–Whitney U test). (F) Percentage of the initial photo-activated signal trafficked to the bacterial pole after 35 seconds in Mock-treated, AIP1-, AIP1+CFL1- or AIP1+GMFB-depleted cells (AIP1 versus MOCK, $P<0.0001$; AIP1 versus AIP1+CFL1, $P<0.0001$; AIP1 versus AIP1+GMFB, $P=0.0005$; Mann–Whitney U test). (G) Proportion of bacteria found in protrusions, vacuoles or free in the cytosol of neighboring cells. Proportion of protrusions: AIP1 versus AIP1+GMFB, $P=0.0016$. Proportion of free bacteria in secondary cell: AIP1 versus AIP1+GMFB, $P<0.0001$. All P -values are calculated using the Mann–Whitney U test. * $P\leq 0.05$; ** $P\leq 0.01$; *** $P\leq 0.001$.

identification of cytoskeleton factors, such as GMFB, TWF2 and CAP1 that genetically interact with AIP1. Similar to CFL1, GMFB and TWF2 are members of the ADF family. Mammalian TWF1, and potentially TWF2, displays capping and severing activity *in vitro* (Poukkula et al., 2011). Yeast (*Saccharomyces cerevisiae*) Gmf1, a homolog of GMFB, displays ARP2/3-specific de-branching activity (Gandhi et al., 2010; Nakano et al., 2010), and its *in vitro* debranching activity was recently shown to be conserved in mammalian GMF γ (Ydenberg et al., 2013). CAP1 is thought to participate in the dissociation of the cofilin–ADP-actin complex (Mattila et al., 2004) and was recently shown to directly enhance cofilin-mediated filament severing (Chaudhry et al., 2013; Normoyle and Briher, 2012). *L. monocytogenes* protrusions therefore are an attractive model system to decipher how the activities of AIP1, CFL1, GMFB, TWF2 and CAP1 contribute to the dynamics of the actin cytoskeleton *in vivo*.

MATERIALS AND METHODS

Bacterial and mammalian cell growth conditions

Listeria monocytogenes strain 10403S was grown overnight in brain heart infusion (BHI) (Difco) supplemented with 10 μ g/ml erythromycin

(Gibco) at 30°C without agitation prior to infection. HeLa 229 cells (ATCC #CCL-2.1) cells were grown in high-glucose Dulbecco's modified Eagle's medium (DMEM) (Invitrogen) supplemented with 10% fetal bovine serum (FBS) (Gibco) at 37°C in a 5% CO₂ incubator.

L. monocytogenes infection

Cells were infected with *L. monocytogenes* strain 10403S expressing GFP or CFP under the control of an IPTG-inducible promoter. The plates were centrifuged at 200 g for 5 minutes and internalization of the bacteria was allowed to proceed for 1 hour at 37°C before gentamicin (50 μ M final) and IPTG (10 mM final) were added in order to kill the remaining extracellular bacteria and induce expression of fluorescent protein genes in internalized bacteria.

Mammalian cell transfection

HeLa 229 cells were transfected using the X-treme gene HP reagent (Roche Applied Science) 24 hours prior to infection. A list of DNA constructs is given in supplementary material Table S2.

Immunofluorescence staining procedures

Cells were seeded on glass coverslips and infected with *L. monocytogenes*. At the appropriate time points, cells were fixed for 20 minutes with 4% formaldehyde in PBS, permeabilized with 0.1%

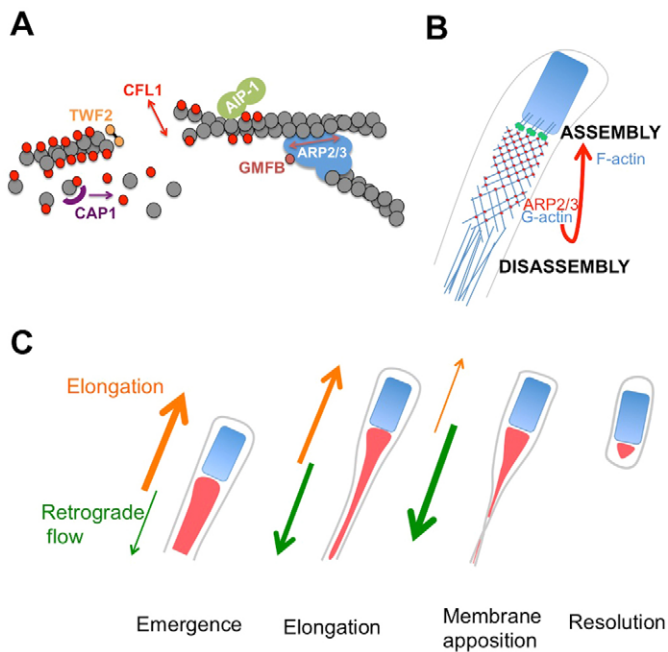


Fig. 7. Model of local recycling of the actin network in *L. monocytogenes* protrusions. (A) Components of the AIP1-dependent disassembly machinery (CFL1, GMFB, TWF2 and CAP1) whose depletion enhances the spreading defect phenotype displayed by AIP1-depleted cells. (B) The bacterial factor ActA (green dots) promotes the nucleation activity of the ARP2/3 complex (red dots), which leads to the assembly of a branched network at the bacterial pole (blue lines and red dots). As protrusions elongate, the AIP1-dependent disassembly machinery recycles G-actin and ARP2/3 from the distal network, which fuels continuous F-actin assembly at the bacterial pole (red arrow). (C) The life cycle of protrusions can be divided in four phases: (1) Emerging protrusions, actin assembly propels the cytosolic bacterium against the plasma membrane, which protrudes into the adjacent cell; (2) elongating protrusions, as protrusions elongate, the disassembly machinery recycles the distal network thereby fuelling further assembly at the bacterial pole in this confined system; (3) stationary protrusions, as the recycling process exhausts the cytoskeleton components from the distal region of protrusions, protrusions become stationary, and continuous actin assembly results in retrograde flow; and (4) protrusion-to-vacuole transition, complete exhaustion of the cytoskeleton components from the distal network allows for membrane apposition in the distal region of protrusions. Continuous generation of forces due to actin assembly and retrograde flow leads to membrane disruption and resolution of the protrusion into a double-membrane vacuole.

Triton X-100 for 5 minutes, blocked for 45 minutes in 3% BSA and incubated overnight at 4°C with primary antibody. Cells were washed in PBS and incubated for 1 hour with the secondary antibody. The samples were then mounted onto glass slides using DABCO antifade reagent. A list of antibodies and concentrations used is given in supplementary material Table S2.

Epifluorescence microscopy

Epi-fluorescence images were acquired using a TE 2000 microscope (Nikon) equipped with a 60× objective (Nikon). Image acquisition and analysis was conducted using the MetaMorph 7.1 software (Molecular Devices).

Confocal microscopy

Images of infected cells were acquired with a Nikon TE2000 spinning disc confocal equipped with a live-cell apparatus and a Micropoint bleaching laser microscope at 37°C in 5% CO₂ (Andor Technology). Analyses were performed with the Volocity software package (Improvision).

Replica electron microscopy

Platinum replica electron microscopy was performed, as described previously (Svitkina, 2007), using an extraction buffer containing 1% Triton X-100, 2 μM phalloidin, 100 mM PIPES pH 6.9, 1 mM EGTA and 1 mM MgCl₂. Before mounting on grids, replicas were additionally treated with Clorox bleach, as described previously (Svitkina and Borisy, 2006), to digest organic material and improve clarity of samples. Samples were analyzed using JEM 1011 transmission electron microscope (JEOL USA, Peabody, MA) operated at 100 kV. Images were captured with an ORIUS 832.10W CCD camera (Gatan, Warrendale, PA) and presented in inverted contrast.

High-throughput imaging and computer-assisted image analysis

384-well plates were imaged using a TE 2000 microscope (Nikon) equipped with a Orca ER Digital CCD Camera (Hamamatsu), motorized stage (Prior), motorized filter wheels (Sutter Instrument, Inc.) and a 10× objective (Nikon) mounted on a Piezo focus drive system (Physik Instrumente). Image acquisition and analysis were conducted using the MetaMorph 7.1 software (Molecular Devices, Inc.). To identify foci of infection, images corresponding to the GFP channel were first thresholded in order to identify objects corresponding to bacteria (see Fig. 1). Infection foci were delineated using the ‘close’ morphology filter of the MetaMorph software (Identification of infection focus, green objects). This step defined regions of interest (ROI) corresponding to infection foci (Fig. 1, thresholded image, yellow line). Within a given ROI, we next used the image morphometry analysis (IMA) module of the MetaMorph software to quantify (1) [Tot] as the total gray intensity values corresponding to the GFP signal, and (2) [Ind] as the gray intensity values corresponding to individual bacteria (Individual bacteria bottom panels). The spreading index, [Ind]/[Tot], represents the proportion of GFP signal represented by individual (and therefore spreading) bacteria within a given infection focus.

RNAi and validation procedures

Cells were transfected by reverse transfection with Dharmafect1 and individual siRNA duplexes (A, B, C and D, 50 nM final) (Dharmacon) or a pool of the four silencing reagents (12.5 nM each, 50 nM total) and incubated for 72 hours. The references of individual siRNA products are given in supplementary material Table S1. For real-time PCR analysis, total RNA and first-strand cDNA synthesis was performed using the TaqMan gene expression Cells-to-Ct kit (Applied Biosystems) as recommended by the manufacturer. Primers were designed using Roche Universal ProbeLibrary Assay Design Center. mRNA was quantified for individual genes as well as a GAPDH internal control using the LightCycler 480 Master Kit and a LightCycler 480 instrument (Roche Biochemicals, Indianapolis, IN). Primers and probe number are given in supplementary material Table S2. For western blot analysis, cells were transfected with the silencing reagents in a 24-well or a 6-well plate format and lysed after 3 days directly in Laemmli sample buffer. A list of antibodies and concentration used is shown in supplementary material Table S2.

Cytosolic actin tail length and F-actin association

Mock- and siRNA-treated HeLa 229 cells were infected for 4 hours, fixed, permeabilized and stained with Alexa-Fluor-568-conjugated phalloidin (1:500) (Invitrogen) and Hoechst 33342 (1:500) (Invitrogen) for 1 hour. Epifluorescence images were acquired, the proportion of bacteria associated with F-actin in the form of a cloud or a polarized tail (supplementary material Fig. S2A) and the length of polarized tails were measured (supplementary material Fig. S2A).

Cytosolic motility

Mock- and siRNA-treated HeLa 229 cells were seeded on day 0 on 35-mm imaging dishes (MatTek). Cells were transfected on day 2 with a given construct (supplementary material Table S2). Cells were infected on day 3 and imaged exclusively from 3 to 6 hours post-infection. Primary infected cells transfected with pDsRed-Monomer-Mem (Clontech) were imaged for 10 minutes with a 444 nm laser (CFP bacteria) and a 561 nm laser (Ds-Red membrane). z-stacks spanning the

entire cell were acquired every 30 second with a spacing of 0.5 μm in the z dimension. The Volocity software package was used to identify bacteria as objects and track them in four dimensions. Each track was manually validated. A speed was obtained for no less than 15 bacteria per treatment, originating from ten cells in three independent experiments.

Protrusion formation and resolution into vacuoles

Mock- and siRNA-treated HeLa 229 cells were seeded on day 0. Cells were transfected with pDsRed-Monomer-Membrane DNA construct (Clontech) on day 2 cells were infected for 5 hours before fixation. Epifluorescence images were acquired and the proportion of bacteria found in protrusions, vacuoles or free in neighboring cells was assessed for no less than 15 primary infected cells in three independent replicates.

Protein localization in protrusions

HeLa 229 cells were seeded on day 0. Cells were transfected with a given construct (supplementary material Table S2) on day 2. Cells were infected on day 3 and fixed after 5 hours. The cells were counterstained with Alexa-Fluor-568-conjugated phalloidin and 5 individual protrusions were imaged per construct. Analyses were restricted to protrusions above 7 μm in length and which had a horizontal orientation (distributed in less than five 0.5 μm z -stack slices). A line profile was calculated from a 0.5- μm -wide line manually drawn on each protrusion from the bacterial pole to the distal end of the protrusions. Line profile intensities were calculated for three channels, corrected to the background fluorescence for each channel and normalized to maximum intensity.

Tracking of proteins during protrusion elongation

Primary infected cells, transfected with a membrane-CFP plasmid (supplementary material Table S2) and a GFP- or YFP-tagged protein construct (supplementary material Table S2), were imaged for 10 minutes with the 444 nm laser and the 490 nm laser. CFP-expressing bacteria and the membrane CFP were acquired simultaneously to avoid excessive photo-bleaching. z -stacks spanning the entire cell were acquired every 40 seconds with a spacing of 0.5 μm in the z dimension. The Volocity software package (Perkin Elmer) was used to correct for photo-bleaching. Individual bacteria undergoing continuous movement (>0.01 $\mu\text{m}/\text{second}$) for at least five successive time points (200 seconds) were identified and selected for analysis. The analysis was restricted to protrusions above 7 μm in length and which had a horizontal orientation (distributed in less than five 0.5 μm z -stack slices). A line profile was calculated from a 0.5- μm -wide line manually drawn on each protrusion and each time point from the bacterial pole to the distal end of the protrusion. Line profile intensities were calculated and corrected with the background fluorescence for each channel. Relative intensity figures were computed by calculating the relative intensity of a signal along the line profile as compared to the maximum intensity in the protrusion at a given time point and for a given fluorophore. Protein distribution profiles were generated for no less than six protrusions in three independent experiments.

Photo-activation and photo-bleaching

Primary infected cells were transfected with a membrane-CFP plasmid (supplementary material Table S2) and a PAGFP-mCherry-tagged β -actin construct (Welman et al., 2010). A Micropoint 404 nm laser (Andor Technology) was used to photo-activate a region of interest (ROI) situated ~ 2 μm from a bacterial pole in protrusions (above 7 μm in length). The ROI surface was kept constant in all experiments. Two pre-activation images were acquired, followed by two recovery images at 2.5-second intervals. The cells were then imaged every 5 seconds for a total of 35 seconds. Laser power and exposure times were kept to a minimum ($<50\%$, <200 milliseconds) to avoid non-specific photo-activation. The localization (cytoplasmic, protrusion) and length of protrusions were assessed visually after the photo-activation experiment by using the membrane CFP marker. The mCherry signal was used to determine the rate of protrusion elongation at the bacterial pole. Images were analyzed using the ImageJ software. The trajectory was drawn along the mCherry signal and used to measure the relative signal intensity

profiles of photo-activated molecules corresponding to the first and last image post-activation (35 s). A kymograph was generated using all images of a given trajectory and used to calculate the speed of retrograde flow.

Photo-bleaching experiments were carried out in cells expressing various fluorescent markers (supplementary material Table S2). Two pre-bleaching images were acquired before the area immediately adjacent to bacteria in protrusion was photo-bleached, and recovery images were captured at maximum speed for 10 seconds. Images in which the bacteria moved outside the constant ROI during the experiment were disregarded. FRAP analysis was conducted with the Volocity software package using a single constrained exponential setting. Three separate independent recovery profiles were generated for each fluorescent marker.

Acknowledgements

We thank Eduardo Groisman, Walther Mothes, Hayley Newton, Avinash Shenoy and the members of the Agaisse laboratory for fruitful discussions and critical reading of the manuscript. We thank Neal Glikman for expert advice on computer-assisted image analysis.

Competing interests

The authors declare no competing interests.

Author contributions

A.M.T. and H.A. conceived the study. A.M.T., R.C., J.C., T.S. and H.A. performed the experiments. All authors read and approved the manuscript.

Funding

This work was funded by the National Institutes of Health [grant numbers R01 GM 095977 to T.S. and R21-AI094228, R01-AI073904 to H.A.]. Deposited in PMC for release after 12 months.

Supplementary material

Supplementary material available online at <http://jcs.biologists.org/lookup/suppl/doi:10.1242/jcs.140038/-DC1>

References

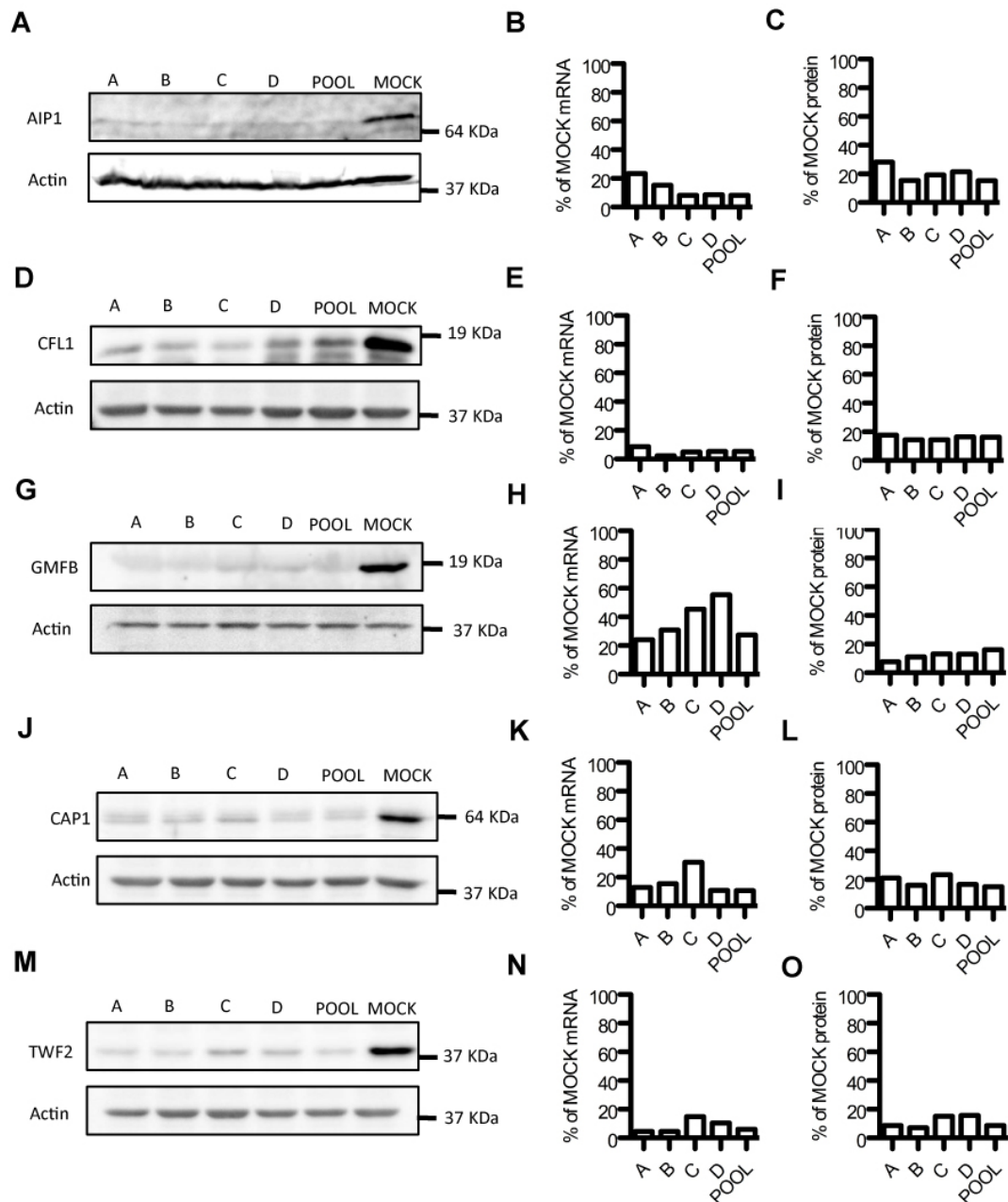
- Andersen, J. B., Roldgaard, B. B., Lindner, A. B., Christensen, B. B. and Licht, T. R. (2006). Construction of a multiple fluorescence labelling system for use in co-invasion studies of *Listeria monocytogenes*. *BMC Microbiol.* **6**, 86.
- Brieher, W. M., Kueh, H. Y., Ballif, B. A. and Mitchison, T. J. (2006). Rapid actin monomer-insensitive depolymerization of *Listeria* actin comet tails by cofilin, coronin, and Aip1. *J. Cell Biol.* **175**, 315–324.
- Chaudhry, F., Breitsprecher, D., Little, K., Sharov, G., Sokolova, O. and Goode, B. L. (2013). Srv2/cyclase-associated protein forms hexameric shurikens that directly catalyze actin filament severing by cofilin. *Mol. Biol. Cell* **24**, 31–41.
- Chong, R., Squires, R., Swiss, R. and Agaisse, H. (2011). RNAi screen reveals host cell kinases specifically involved in *Listeria monocytogenes* spread from cell to cell. *PLoS ONE* **6**, e23399.
- Domann, E., Wehland, J., Rohde, M., Pistor, S., Hartl, M., Goebel, W., Leimeister-Wächter, M., Wuenschel, M. and Chakraborty, T. (1992). A novel bacterial virulence gene in *Listeria monocytogenes* required for host cell microfilament interaction with homology to the proline-rich region of vinculin. *EMBO J.* **11**, 1981–1990.
- Forscher, P. and Smith, S. J. (1988). Actions of cytochalasins on the organization of actin filaments and microtubules in a neuronal growth cone. *J. Cell Biol.* **107**, 1505–1516.
- Gandhi, M., Smith, B. A., Bovellan, M., Paavilainen, V., Daugherty-Clarke, K., Gelles, J., Lappalainen, P. and Goode, B. L. (2010). GMF is a cofilin homologue that binds Arp2/3 complex to stimulate filament debranching and inhibit actin nucleation. *Curr. Biol.* **20**, 861–867.
- Haglund, C. M. and Welch, M. D. (2011). Pathogens and polymers: microbe-host interactions illuminate the cytoskeleton. *J. Cell Biol.* **195**, 7–17.
- Kocks, C., Guoin, E., Tabouret, M., Berche, P., Ohayon, H. and Cossart, P. (1992). *Listeria monocytogenes*-induced actin assembly requires the actA gene product, a surface protein. *Cell* **68**, 521–531.
- Lambrechts, A., Gevaert, K., Cossart, P., Vandekerckhove, J. and Van Troys, M. (2008). *Listeria* comet tails: the actin-based motility machinery at work. *Trends Cell Biol.* **18**, 220–227.
- Lasa, I., Guoin, E., Goethals, M., Vancompernelle, K., David, V., Vandekerckhove, J. and Cossart, P. (1997). Identification of two regions in the N-terminal domain of ActA involved in the actin comet tail formation by *Listeria monocytogenes*. *EMBO J.* **16**, 1531–1540.
- Loisel, T. P., Boujemaa, R., Pantaloni, D. and Carlier, M.-F. (1999). Reconstitution of actin-based motility of *Listeria* and *Shigella* using pure proteins. *Nature* **401**, 613–616.

- Mattila, P. K., Quintero-Monzon, O., Kugler, J., Moseley, J. B., Almo, S. C., Lappalainen, P. and Goode, B. L.** (2004). A high-affinity interaction with ADP-actin monomers underlies the mechanism and in vivo function of Srv2/cyclase-associated protein. *Mol. Biol. Cell* **15**, 5158–5171.
- Mohri, K., Ono, K., Yu, R., Yamashiro, S. and Ono, S.** (2006). Enhancement of actin-depolymerizing factor/cofilin-dependent actin disassembly by actin-interacting protein 1 is required for organized actin filament assembly in the *Caenorhabditis elegans* body wall muscle. *Mol. Biol. Cell* **17**, 2190–2199.
- Nakano, K., Kuwayama, H., Kawasaki, M., Numata, O. and Takaine, M.** (2010). GMF is an evolutionarily developed Adf/cofilin-super family protein involved in the Arp2/3 complex-mediated organization of the actin cytoskeleton. *Cytoskeleton* **67**, 373–382.
- Normoyle, K. P. M. and Briehner, W. M.** (2012). Cyclase-associated protein (CAP) acts directly on F-actin to accelerate cofilin-mediated actin severing across the range of physiological pH. *J. Biol. Chem.* **287**, 35722–35732.
- Pollard, T. D. and Borisy, G. G.** (2003). Cellular motility driven by assembly and disassembly of actin filaments. *Cell* **112**, 453–465.
- Poukkula, M., Kremneva, E., Serlachius, M. and Lappalainen, P.** (2011). Actin-depolymerizing factor homology domain: a conserved fold performing diverse roles in cytoskeletal dynamics. *Cytoskeleton* **68**, 471–490.
- Robbins, J. R., Barth, A. I., Marquis, H., de Hostos, E. L., Nelson, W. J. and Theriot, J. A.** (1999). *Listeria monocytogenes* exploits normal host cell processes to spread from cell to cell. *J. Cell Biol.* **146**, 1333–1350.
- Rolls, M. M., Stein, P. A., Taylor, S. S., Ha, E., McKeon, F. and Rapoport, T. A.** (1999). A visual screen of a GFP-fusion library identifies a new type of nuclear envelope membrane protein. *J. Cell Biol.* **146**, 29–44.
- Sechi, A. S., Wehland, J. and Small, J. V.** (1997). The isolated comet tail pseudopodium of *Listeria monocytogenes*: a tail of two actin filament populations, long and axial and short and random. *J. Cell Biol.* **137**, 155–167.
- Siripala, A. D. and Welch, M. D.** (2007). SnapShot: actin regulators I. *Cell* **128**, 626.e1–626.e2.
- Skoble, J., Portnoy, D. A. and Welch, M. D.** (2000). Three regions within ActA promote Arp2/3 complex-mediated actin nucleation and *Listeria monocytogenes* motility. *J. Cell Biol.* **150**, 527–538.
- Stevens, J. M., Galyov, E. E. and Stevens, M. P.** (2006). Actin-dependent movement of bacterial pathogens. *Nat. Rev. Microbiol.* **4**, 91–101.
- Svitkina, T.** (2007). Electron microscopic analysis of the leading edge in migrating cells. *Methods Cell Biol.* **79**, 295–319.
- Svitkina, T. M. and Borisy, G. G.** (2006). Correlative light and electron microscopy of the cytoskeleton. In *Cell Biology*, 3rd edn (ed. E. C. Julio), pp. 277–285. Burlington, MA: Academic Press.
- Theriot, J. A., Mitchison, T. J., Tilney, L. G. and Portnoy, D. A.** (1992). The rate of actin-based motility of intracellular *Listeria monocytogenes* equals the rate of actin polymerization. *Nature* **357**, 257–260.
- Wang, Y. L.** (1985). Exchange of actin subunits at the leading edge of living fibroblasts: possible role of treadmilling. *J. Cell Biol.* **101**, 597–602.
- Welch, M. D., Iwamatsu, A. and Mitchison, T. J.** (1997). Actin polymerization is induced by Arp2/3 protein complex at the surface of *Listeria monocytogenes*. *Nature* **385**, 265–269.
- Welch, M. D., Rosenblatt, J., Skoble, J., Portnoy, D. A. and Mitchison, T. J.** (1998). Interaction of human Arp2/3 complex and the *Listeria monocytogenes* ActA protein in actin filament nucleation. *Science* **281**, 105–108.
- Welman, A., Serrels, A., Brunton, V. G., Ditzel, M. and Frame, M. C.** (2010). Two-color photoactivatable probe for selective tracking of proteins and cells. *J. Biol. Chem.* **285**, 11607–11616.
- Ydenberg, C. A., Padrick, S. B., Sweeney, M. O., Gandhi, M., Sokolova, O. and Goode, B. L.** (2013). GMF severs actin-Arp2/3 complex branch junctions by a cofilin-like mechanism. *Curr. Biol.* **23**, 1037–1045.

Actin network disassembly powers *Listeria monocytogenes* dissemination

Arthur M. Talman¹, Ryan Chong¹, Jonathan Chia², Tatyana Svitkina² and Hervé Agaisse^{1*}

SUPPLEMENTARY FIGURES



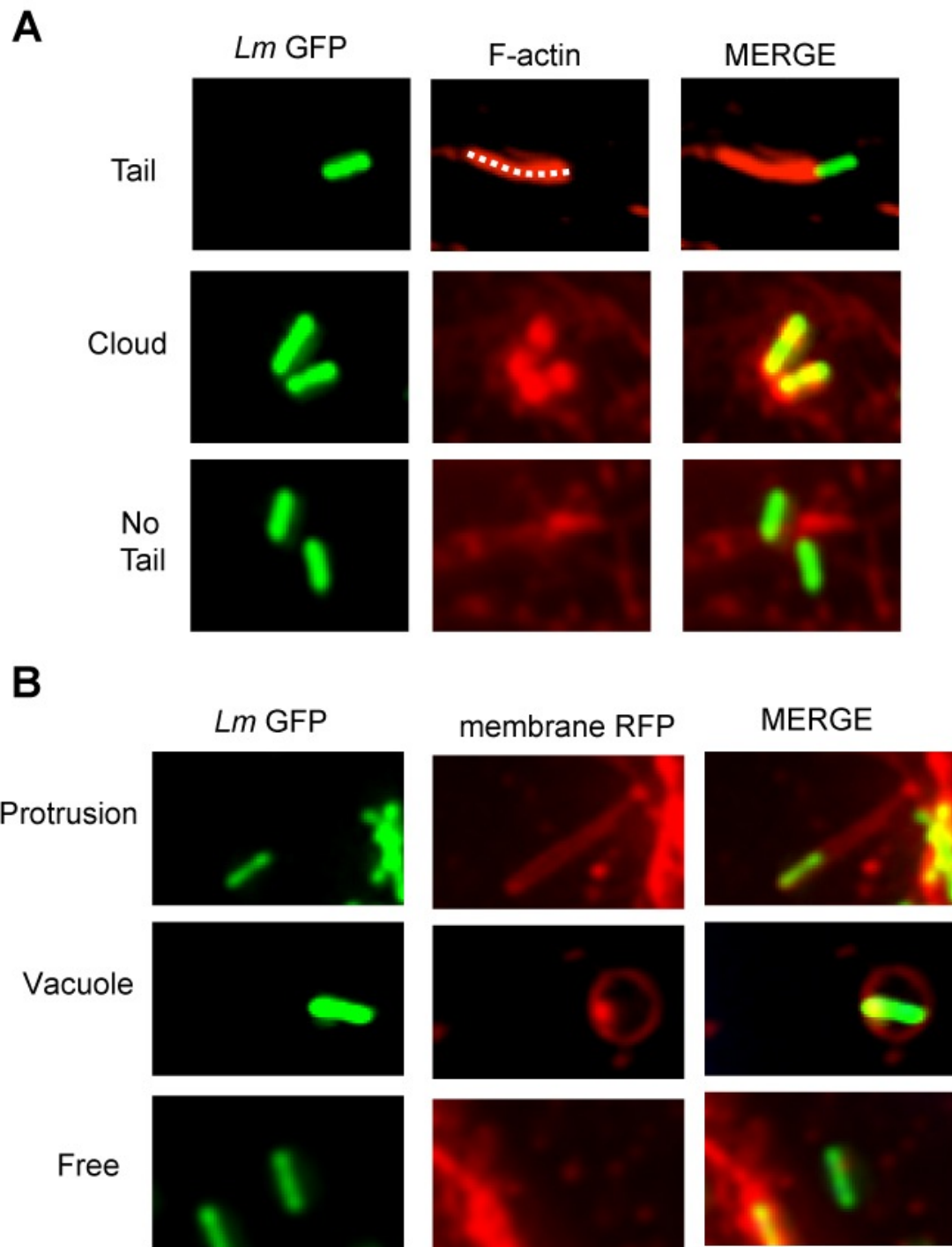


Figure S2. Analysis of cytosolic actin comet tails and membrane protrusion formation

(A) HeLa cells infected with GFP-expressing *L. monocytogenes* for 4 hours, fixed and stained with Phalloidin-Alexa 568. The length of polarized tails (tail, white dashed line) and the proportion of bacteria associated with F-actin (tail and cloud) were determined. (B) Cells transfected with a membrane-targeted dsRed-expressing construct and infected with GFP-expressing *L. monocytogenes*. After 6 hours of

infection, samples were fixed and primary infected cells were imaged. The proportion of bacteria in neighboring cells associated with membrane-targeted dsRed in protrusions, vacuoles or not associated with the membrane marker (free) was determined.

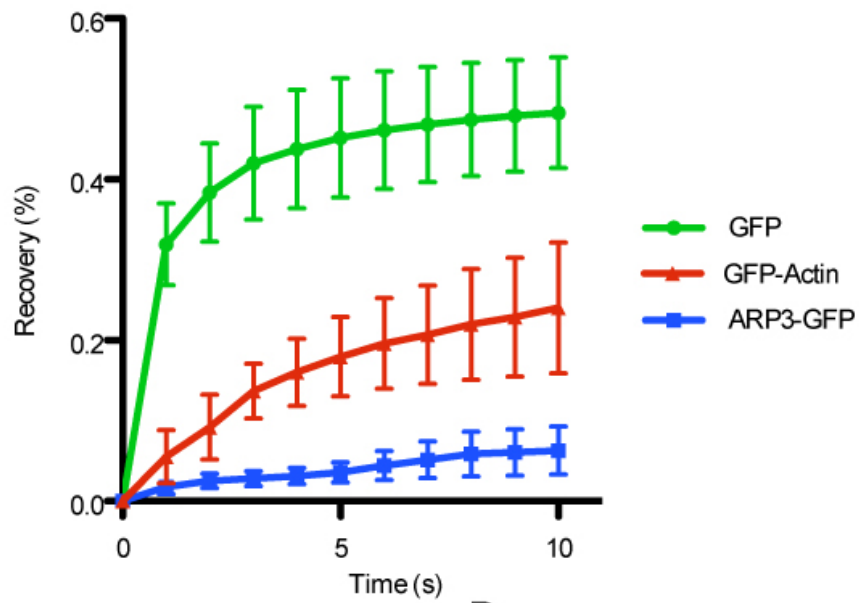
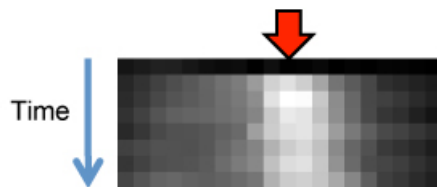
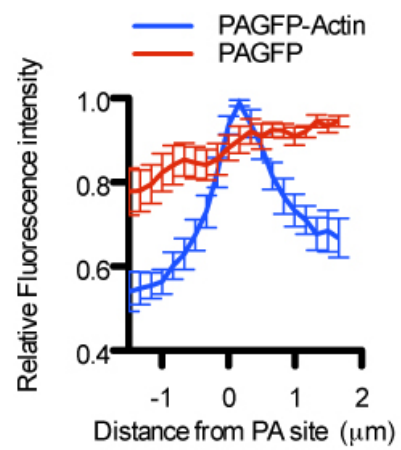
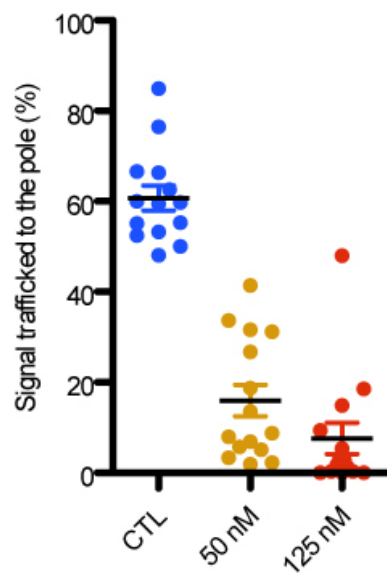
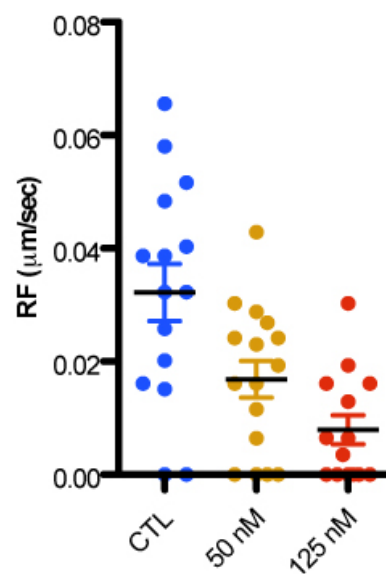
A**B****C****D****E****F**

Figure S3. Diffusion and dynamics of actin network components in protrusions.

(A) Analysis of fluorescence recovery after photobleaching (FRAP) of GFP, GFP-Actin and ARP3-GFP. Photo-bleaching the proximal network at the bacterial pole led to only 47 % recovery of the signal corresponding to free GFP (half time 0.7 sec). The signal corresponding to GFP-Actin displayed only 25% recovery and the recovery rate was markedly slower than the rate observed for free GFP (half time 3.0 sec). The signal corresponding to ARP3-GFP hardly recovered (11 %, half time 8.7 sec), showing that the pool of ARP2/3 located at the bacterial pole is finite in protrusions. These FRAP experiments indicate that the protrusion is a confined environment that receives very little contribution from cytosolic materials. (B and C) Kymographs representing the evolution of the photo-activated signal (red arrow, site of photo-activation) in protrusion space over a 5 second period (blue arrow, time) for PAGFP-Actin (B) and free GFP (C). (D) Intensity profiles for 10 independent kymograph analyses as shown in B (red line) and C (blue line). The experiments indicate that, over a 5 second period, free GFP was distributed in the whole protrusion space, whilst photo-activated Actin-GFP remained confined to the site of photo-activation. These results support the notion that (photo-activatable) GFP-Actin is incorporated in an actin network in protrusions, and its slow disappearance reflects the relatively slow disassembly of the actin network and fast diffusion of the released components. (E-F) Dose-dependent effect of increasing concentrations of cytochalasin D indicating that the amount of photo-activated actin trafficked to the bacterial pole (E) and the rate of retrograde flow (F), reflect the efficiency of actin assembly.

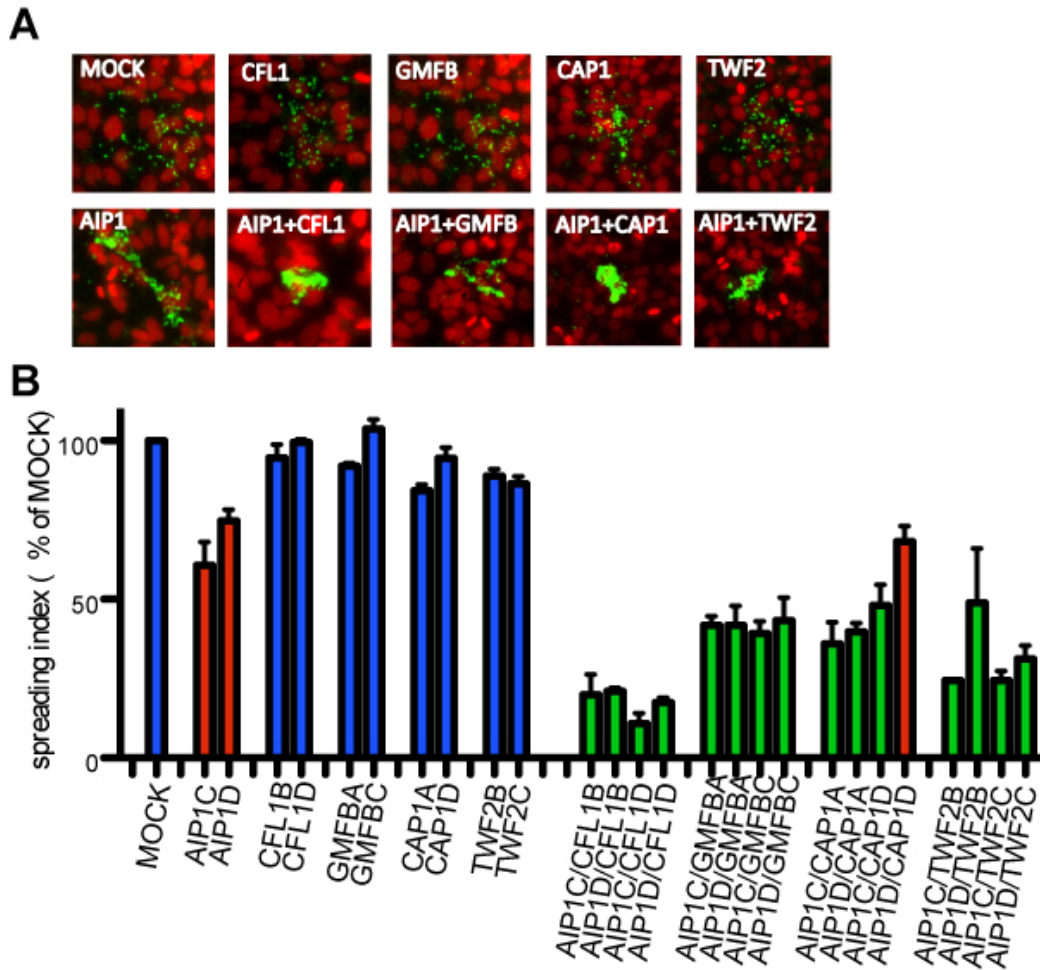


Figure S4. Components of the AIP1-dependent disassembly machinery.

(A) Representative infection foci in mock-treated, AIP1-, CFL-, GMFB-, CAP1-, TWf2-, AIP1/CFL1-, AIP1/GMFB-, AIP1/CAP1- and AIP1/TWf2-depleted HeLa 229 cells, after 8 hours of infection with GFP-expressing *L. monocytogenes* and stained with DAPI (red). (B) Graph displaying spreading index values observed in cells treated with 2 different siRNA duplexes alone or in heterologous combination of AIP1, CFL1, GMFB, CAP1 or TWf2. Red bars represent spreading indexes significantly different from MOCK (blue) and green bars represent spreading indexes significantly different from AIP1 siRNA duplexes C or D.



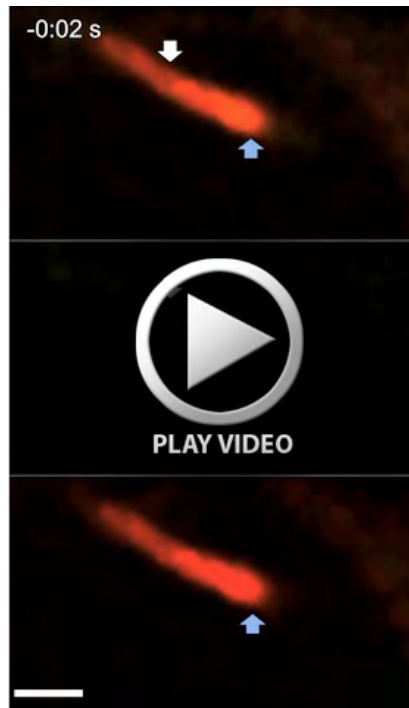
Movie S1. Protrusion formation and resolution into double membrane vacuole. Time-lapse microscopy of a HeLa229 cell transfected with membrane-targeted dsRed (red) and infected with GFP-expressing *L. monocytogenes*. The protrusion first elongates, becomes stationary and finally resolves into a double membrane vacuole. Scale bar 5 μm .



Movie S2. Tracking ARP2/3 distribution in protrusions. Time-lapse microscopy of a HeLa229 cell transfected with membrane-targeted CFP (cyan) and ARP3-GFP (pseudo-colored yellow) and infected with CFP-expressing *L. monocytogenes*. The protrusion on the left is stationary whilst the protrusion on the right is elongating. Note the redistribution of ARP3-GFP in the protrusion on the right, as it elongates towards the left. Scale bar 2 μm .



Movie S3. Dynamics of the actin network in a cytosolic tail. Photo-activation of mCherry-Actin (red) fused to photo-activatable GFP (pseudo-colored yellow) in a cytosolic *Listeria monocytogenes* actin tail as shown in Fig. 5A. The white arrow indicates the site of photo-activation and the blue arrow indicates the initial position of the bacterial pole. The intensity of the photo-activated signal decreases at the site of photo-activation, as a result of actin network disassembly. Note the expansion of the actin network (red channel) on the right side of the blue arrow, reflecting the assembly of the actin tail. Scale bar 2 μm .



Movie S4. Dynamics of the actin network in an elongating protrusion. Photo-activation of mCherry Actin (red) fused to photo-activatable GFP (pseudocolored yellow) in an elongating *Listeria monocytogenes* protrusion as shown in Fig. 5B. The white arrow indicates the site of photo-activation and the blue arrow indicates the initial position of the bacterial pole. The intensity of the photo-activated signal decreases at the site of photo-activation, as a result of actin network disassembly and increases at the bacterial pole, as a result of photo-activated actin assembly. Note the expansion of the actin network on the right side of the blue arrow, showing that the protrusion elongates. Scale bar 2 μm .



Movie S5. Dynamics of the actin network in a stationary protrusion. Photo-activation of mCherry-Actin (red) fused to photo-activatable GFP (pseudocolored yellow) in a stationary *Listeria monocytogenes* protrusion as shown in Fig. 5C. The white arrow indicates the site of photo-activation and the blue arrow indicates the initial position of the bacterial pole. The photo-activated signal drifts backwards on the left side of the white arrow, as a result of retrograde flow, and decreases in intensity, as a result of actin network disassembly. The intensity of the photo-activated signal increases at the bacterial pole, as a result of photo-activated actin assembly. Note the absence of expansion of the actin network on the right side of the blue arrow, showing that the protrusion is stationary. Scale bar 2 μm .

Actin network disassembly powers *Listeria monocytogenes* dissemination

Arthur M. Talman¹, Ryan Chong¹, Jonathan Chia², Tatyana Svitkina² and Hervé Agaisse^{1*}

SUPPLEMENTARY TABLES

Gene symbol	Ensembl accession	50 nM				25 nM				25 nM + 25 mM siAIP-1			
		A	B	C	D	A	B	C	D	A	B	C	D
DIAPH1	ENSG00000131504	95	89	97	85	98	93	103	103	101	102	102	125
DIAPH2	ENSG00000147202	95	95	105	86	102	108	108	53	99	88	125	78
DIAPH3	ENSG00000139734	99	97	103	97	109	107	111	101	118	108	128	112
FHOD1	ENSG00000135723	200	99	92	91	105	103	99	94	96	89	82	115
FHOD2	ENSG00000157827	89	102	85	94	100	104	58	107	85	98	83	73
FHOD3	ENSG00000134775	94	99	95	90	104	79	105	91	98	102	124	39
FMN1	ENSG00000248905	94	94	100	86	96	77	109	101	100	122	118	95
FMN2	ENSG00000155816	90	91	91	75	90	99	98	95	117	89	100	100
FMNL1	ENSG00000184922	62	81	75	97	48	104	96	103	75	114	126	110
FMNL2	ENSG00000157827	98	94	94	97	86	98	95	104	103	97	92	97
FMNL3	ENSG00000161791	99	111	88	102	103	123	99	100	88	146	106	121
INF2	ENSG00000203485	64	103	102	96	83	99	108	86	107	130	77	114
GRID2IP	ENSG00000215045	68	95	64	106	58	101	96	101	104	120	93	104
ACTR2	ENSG00000138071	74	94	2	9	11	2	12	3	42	4	5	6
ACTR3	ENSG00000115091	11	46	50	29	5	57	43	19	7	50	87	8
ARPC1A	ENSG00000241685	95	94	85	96	103	104	105	98	53	95	118	138
ARPC1B	ENSG00000130429	57	92	97	86	67	104	102	48	77	46	107	77
ARPC2	ENSG00000163466	3	33	3	7	3	38	64	20	2	15	4	17
ARPC3	ENSG00000111229	2	40	98	28	38	32	98	4	5	2	132	1
ARPC4	ENSG00000241553	6	18	12	5	6	9	20	36	29	14	26	27
ARPC5	ENSG00000162704	87	104	96	86	83	105	102	98	72	99	75	75
SPIRE1	ENSG00000134278	97	97	93	66	98	96	94	67	124	114	122	47
SPIRE2	ENSG00000204991	71	98	94	84	78	108	95	96	82	110	126	102
LRRC16A	ENSG00000079691	84	96	94	92	69	103	81	98	106	93	80	88
CORO1A	ENSG00000102879	93	97	84	96	75	96	80	79	83	130	63	114
CORO1B	ENSG00000172725	94	75	88	79	103	81	94	94	106	94	109	79
CORO1C	ENSG00000110880	94	100	84	97	92	109	85	85	110	122	100	135
CORO2A	ENSG00000106789	98	87	82	98	90	112	87	112	110	66	103	116
CORO2B	ENSG00000103647	81	92	89	81	97	83	86	90	118	86	53	84
CORO6	ENSG00000167549	96	91	100	75	90	107	112	79	122	118	129	99
CORO7	ENSG00000103426	85	93	71	85	94	99	107	103	90	50	131	73
EZR	ENSG00000092820	90	106	106	104	113	104	103	108	122	126	116	150
CTTN	ENSG00000085733	95	106	97	91	104	92	111	96	140	144	104	126
WASF1	ENSG00000112290	96	95	100	98	106	104	110	107	138	88	115	124
WASF2	ENSG00000158195	101	94	100	95	99	113	109	111	128	75	115	130
WASF3	ENSG00000132970	104	80	74	96	109	79	74	103	122	60	58	97
WAS	ENSG00000015285	101	91	90	99	75	101	96	103	109	105	96	122
WASL	ENSG00000106299	101	104	101	93	97	110	108	112	127	121	107	141
WHAMM	ENSG00000156232	89	74	86	70	106	112	91	108	102	113	104	138
CAP1	ENSG00000131236	74	101	103	92	92	100	103	102	75	120	81	74
CAP2	ENSG00000112186	93	99	97	94	106	100	107	94	119	127	127	131
PFN1	ENSG00000108518	84	86	99	96	89	92	108	98	106	110	102	126
PFN2	ENSG00000070087	96	86	101	99	109	93	112	113	107	118	97	148
PFN3	ENSG00000196570	77	103	99	101	89	102	104	107	105	137	125	172
PFN4	ENSG00000176732	90	92	101	104	73	106	102	102	102	135	106	130
TMSB4X	ENSG00000205542	90	92	96	91	99	98	98	100	90	109	117	118
WIPF1	ENSG00000115935	96	103	97	88	98	109	105	107	70	112	106	130
WIPF2	ENSG00000171475	99	91	89	97	104	101	109	78	130	130	122	113
WIPF3	ENSG00000122574	98	97	81	96	110	109	87	97	106	113	108	101

Gene symbol	Ensembl accession	50 nM				25 nM				25 nM + 25 mM siAIP-1			
		A	B	C	D	A	B	C	D	A	B	C	D
ENAH	ENSG00000154380	93	92	99	104	114	102	103	109	117	113	133	95
VASP	ENSG00000125753	94	93	84	101	88	106	109	113	108	109	96	117
EVL	ENSG00000196405	<u>44</u>	<u>94</u>	<u>100</u>	<u>88</u>	<u>9</u>	<u>112</u>	<u>101</u>	<u>106</u>	92	118	91	131
WDR1	ENSG00000071127	<u>74</u>	<u>76</u>	<u>69</u>	<u>73</u>	<u>69</u>	<u>94</u>	<u>66</u>	<u>80</u>	<u>60</u>	<u>107</u>	<u>105</u>	<u>100</u>
CAPG	ENSG00000042493	99	102	97	98	105	108	108	105	111	109	99	111
CAPZA1	ENSG00000116489	<u>63</u>	<u>78</u>	<u>90</u>	<u>89</u>	80	78	94	100	<u>82</u>	<u>52</u>	<u>38</u>	<u>54</u>
CAPZA2	ENSG00000198898	106	96	93	89	115	102	105	108	132	96	131	101
CAPZA3	ENSG00000177938	96	98	95	88	102	107	106	93	<u>104</u>	<u>132</u>	<u>126</u>	<u>69</u>
CAPZB	ENSG00000077549	<u>31</u>	<u>47</u>	<u>31</u>	<u>60</u>	<u>26</u>	<u>24</u>	<u>42</u>	<u>58</u>	<u>22</u>	<u>104</u>	<u>45</u>	<u>26</u>
CFL1	ENSG00000172757	85	85	82	90	<u>91</u>	<u>95</u>	<u>39</u>	<u>96</u>	<u>38</u>	<u>38</u>	<u>54</u>	<u>44</u>
CFL2	ENSG00000165410	90	106	82	87	88	109	87	104	<u>98</u>	<u>148</u>	<u>98</u>	<u>74</u>
DSTN	ENSG00000125868	91	81	99	85	104	95	97	82	<u>90</u>	<u>54</u>	<u>116</u>	<u>91</u>
GSN	ENSG00000148180	92	81	102	104	92	106	94	102	120	86	109	128
VIL1	ENSG00000127831	<u>103</u>	<u>98</u>	<u>64</u>	<u>105</u>	110	98	81	93	115	119	104	111
VILL	ENSG00000136059	104	101	97	105	107	103	105	105	106	96	121	131
SVIL	ENSG00000197321	93	83	91	99	103	94	111	131	101	124	108	138
SCN	ENSG00000075142	99	84	106	102	112	101	123	93	124	94	136	114
FLII	ENSG00000177731	<u>88</u>	<u>70</u>	<u>95</u>	<u>102</u>	<u>86</u>	<u>53</u>	<u>104</u>	<u>108</u>	79	81	127	106
AVIL	ENSG00000135407	87	100	100	94	98	115	105	99	137	151	126	98
TWF1	ENSG00000151239	90	90	98	94	97	106	97	107	105	81	82	128
TWF2	ENSG00000247596	<u>87</u>	<u>77</u>	<u>85</u>	<u>76</u>	107	80	86	82	<u>106</u>	<u>55</u>	<u>26</u>	<u>78</u>
ACTN1	ENSG00000072110	99	86	86	97	103	77	101	105	77	93	104	96
ACTN2	ENSG00000077522	102	101	97	101	101	103	103	103	127	90	139	90
ACTN3	ENSG00000248746	84	87	84	82	106	93	103	93	106	85	102	102
ACTN4	ENSG00000130402	<u>99</u>	<u>81</u>	<u>88</u>	<u>50</u>	<u>96</u>	<u>92</u>	<u>110</u>	<u>40</u>	<u>112</u>	<u>98</u>	<u>126</u>	<u>50</u>
FSCN1	ENSG00000075618	<u>98</u>	<u>73</u>	<u>86</u>	<u>91</u>	100	110	101	87	121	104	92	101
FSCN2	ENSG00000186765	104	85	97	93	97	105	110	91	<u>84</u>	<u>57</u>	<u>137</u>	<u>115</u>
FSCN3	ENSG00000106328	100	98	84	99	103	100	111	107	99	97	134	95
FLNA	ENSG00000196924	<u>100</u>	<u>103</u>	<u>80</u>	<u>91</u>	110	112	95	96	104	144	95	93
FLNB	ENSG00000136068	<u>74</u>	<u>99</u>	<u>85</u>	<u>96</u>	99	92	96	102	100	87	99	97
FLNC	ENSG00000128591	<u>80</u>	<u>95</u>	<u>74</u>	<u>68</u>	77	94	85	102	81	111	125	85
PLS1	ENSG00000120756	<u>86</u>	<u>86</u>	<u>61</u>	<u>70</u>	<u>99</u>	<u>103</u>	<u>92</u>	<u>68</u>	101	103	91	86
LCP1	ENSG00000136167	93	94	90	89	100	108	85	103	<u>92</u>	<u>117</u>	<u>96</u>	<u>73</u>
PLS3	ENSG00000102024	<u>92</u>	<u>88</u>	<u>105</u>	<u>79</u>	100	95	102	80	130	127	113	106
SPTBN2	ENSG00000173898	<u>99</u>	<u>72</u>	<u>71</u>	<u>97</u>	<u>93</u>	<u>89</u>	<u>72</u>	<u>106</u>	103	116	83	114
SPTAN1	ENSG00000197694	103	100	94	91	101	97	103	93	95	117	106	101
SPTBN1	ENSG00000115306	<u>94</u>	<u>42</u>	<u>102</u>	<u>106</u>	<u>99</u>	<u>60</u>	<u>94</u>	<u>104</u>	<u>75</u>	<u>82</u>	<u>92</u>	<u>104</u>
SPTBN4	ENSG00000160460	97	105	90	91	107	104	89	108	<u>112</u>	<u>96</u>	<u>74</u>	<u>94</u>
SPTBN5	ENSG00000137877	<u>100</u>	<u>36</u>	<u>63</u>	<u>87</u>	<u>106</u>	<u>44</u>	NA	<u>95</u>	<u>87</u>	<u>34</u>	<u>24</u>	<u>100</u>
GMF B	ENSG00000197045	<u>89</u>	<u>85</u>	<u>99</u>	<u>71</u>	<u>90</u>	<u>87</u>	<u>93</u>	<u>56</u>	<u>51</u>	<u>64</u>	<u>59</u>	<u>73</u>
GMF G	ENSG00000130755	115	96	88	96	108	105	97	97	142	105	90	145

Table S1. RNAi screen for cytoskeleton factors required for *Listeria monocytogenes* spread from cell to cell. The siRNA library was screened in three independent replicates, at two different concentrations, and in combination with AIP1. Note that values for 50nM and 25nM are given as percentage relative to the spreading index observed in mock-treated cells. Note that values for 25 nM + 25 nM siAIP1 are given as percentage relative to the spreading index observed in AIP1-depleted cells. Thus, a value of 100 for 25 nM+ 25 nM siAIP1 indicates no change with respect to the spreading index observed in cells treated with 25nM AIP1 siRNA C. Values deviating from the mean by at least 2 standard deviation units with respect to the appropriate control are underlined. 4 individual siRNA duplexes were tested per gene.

Highlighted are genes displaying a significantly different value for one duplex (Green), two duplexes (Blue), three duplexes (Orange), four duplexes (Red).

qPCR primers			
Primer sequence (5' -> 3')	Forward (F) or reverse (R)	Gene	Probe number (Roche Unoversal probe library)
tggaagatcaaagacattgc	F	AIP1	7
ccagaggaagactgctcca	R	AIP1	7
gtgccctctcctttcgttt	F	CFL1	5
ttgaacaccttgatgacacat	R	CFL1	5
tttattttctccagtcctgttg	F	GMFB	11
cttggttagttcagctgtctgg	R	GMFB	12
ctggagatcgccaagaaaat	F	TWF2	43
gcacctcgctgtagaggaact	R	TWF2	43
tctaccagttcaggctcagatg	F	CAP1	38
gggcagggttctgtgagt	R	CAP1	38
Cloning primers			
Primer sequence (5' -> 3')	Primer name	Gene	
aagaagcttacataaggaggaactactatgagcgggggagaggag c	bCFP F	CFP (codon optimised)	
gcagcatgcaatttttagcggtagctcgtccatgc	bCFP R	CFP (codon optimised)	
aatactcgagttacgacatgactccaacactggatt	ARP3 F	human ARP3	
aataggatccatggcgggacggctgccgcctgtg	ARP3 R	human ARP3	
ctcgagctatgccgtacgagatcaag	AIPF	human AIP1 isoform 1	
ggatcctcatcagtaggtgattgtccac	AIPR	human AIP1 isoform 1	
cggtgcataaaaacggcggaaaatcctacattactctgggag	AIP res 1F	human AIP1 isoform 1	
gtgccagagtaaatgtaggattttccgccgttttatgaccg	AIP res 1R	human AIP1 isoform 1	
cataaaaacggcggaaaatcttatattactctgggagccacg	AIP res 2F	human AIP1 isoform 1	
cgtggctcccagagtaaatataagattttccgccgttttatg	AIP res 2R	human AIP1 isoform 1	
gggaaggaaggcgaagtctcgagc	AIP E125A F	human AIP1 isoform 1, E125A	
gctccaaactcgccctccttccc	AIP E125A R	human AIP1 isoform 1, E125A	
ccacgggaagcgtgataactgcg	AIP D167A F	human AIP1 isoform 1, D167A	
gcgagttatcagcgttcccgtgg	AIP D167A R	human AIP1 isoform 1, D167A	
gaccccatcaaggccaagttcacaattgg	AIP F181A F	human AIP1 isoform 1, F181A	
ccaattgtgaactggcctgaatgggggtc	AIP F181A R	human AIP1 isoform 1, F181A	
caattggcgaccacagccgctgcaactgtgtgcgattc	AIP F191 A F	human AIP1 isoform 1, F191A	
gaatcgcacacagttgacagcggctgtggtcgccaattg	AIP F191 A F	human AIP1 isoform 1, F191A	

Target protein	Company	Species	Catalog number	Immuno-fluorescence primary incubation concentration	Western blotting primary incubation concentration
Primary					
ARP3	Millipore	Rabbit	07-272	1 in 400	1 in 1000
AIP1	Santa Cruz Biotechnology	Goat	sc-160907	1 in 100	1 in 500
CFL1	Abcam	Rabbit	42824	1 in 1000	1 in 5000
TWF2	Santa Cruz Biotechnology	Rabbit	sc-100216	1 in 100	1 in 1000
CAP1	Santa Cruz Biotechnology	Mouse	sc-376512	1 in 100	1 in 1000
Secondary					
Alexa Fluor 514 Goat Anti-Rabbit	Invitrogen	Goat	A31558	1 in 2000	NA
Alexa Fluor 514 Goat Anti-Mouse IgG	Invitrogen	Goat	A31555	1 in 2000	NA
Alexa Fluor 488 Donkey Anti-Goat IgG	Invitrogen	Donkey	A11055	1 in 2000	NA
Peroxidase conjugated anti-Goat IgG	Jackson ImmunoResearch	Donkey	705-035-147	NA	1 in 20 000
Peroxidase conjugated anti-Rabbit IgG	Jackson ImmunoResearch	Goat	111-035-144	NA	1 in 10 000
Peroxidase conjugated anti-Mouse IgG	Jackson ImmunoResearch	Goat	115-035-146	NA	1 in 10 000

Plasmids	Obtained or generated	Source	Cloning strategy
p315 HSPK CFP	Generated		Amplified CFP from JEBAN2 (Andersen et al., 2006) and cloned into p315 HSPK GFP into SphI and HindIII restriction sites (partial digest)
membrane targeted dsRed	Obtained	Clontech	NA
mCFP	Generated		cloned from eCFP plasmid (Clontech) into KasI and NotI restriction sites
ARP3-GFP	Generated		Amplified from HeLa cell cDNA and cloned into pEGFP - N1 (clontech) into XhoI and BamHI restriction sites
YFP-Actin	Obtained	(Rolls et al., 1999)	NA
GFP-AIP1	Generated		Amplified from HeLa cell cDNA and cloned into pEGFP-C1 (Clontech) into XhoI and BamHI restriction sites. Introduced synonymous mutations by site-directed mutagenesis to render resistant to siRNA C
GFP-AIP1mut	Generated	(Mohri et al., 2006)	GFP-AIP1 was modified by introducing 4 different mutations in the coding sequence of AIP-1 by site directed mutagenesis (E125A, D167A, F181A, F191A) (Mohri et al., 2006)
CFL1-GFP	Generated		Amplified from HeLa cell cDNA and cloned into pEGFP - N1 (clontech) into XhoI and BamHI restriction sites
PAGFP mcherry Actin	Obtained	Kind gift from A. Welman (Welman et al., 2010)	NA

Table S2. Oligonucleotides, antibodies and plasmids used in this study.

References

Andersen, J., Roldgaard, B., Lindner, A., Christensen, B. and Licht, T. (2006). Construction of a multiple fluorescence labelling system for use in co-invasion studies of *Listeria monocytogenes*. *BMC Microbiology* **6**, 86.

Mohri, K., Ono, K., Yu, R., Yamashiro, S. and Ono, S. (2006). Enhancement of Actin-depolymerizing Factor/Cofilin-dependent Actin Disassembly by Actin-interacting Protein 1 Is Required for Organized Actin Filament Assembly in the *Caenorhabditis elegans* Body Wall Muscle. *Molecular Biology of the Cell* **17**, 2190-2199.

Rolls, M. M., Stein, P. A., Taylor, S. S., Ha, E., McKeon, F. and Rapoport, T. A. (1999). A Visual Screen of a Gfp-Fusion Library Identifies a New Type of Nuclear Envelope Membrane Protein. *The Journal of Cell Biology* **146**, 29-44.

Welman, A., Serrels, A., Brunton, V. G., Ditzel, M. and Frame, M. C. (2010). Two-color Photoactivatable Probe for Selective Tracking of Proteins and Cells. *Journal of Biological Chemistry* **285**, 11607-11616.